Nanoscale

PAPER

View Article Online
View Journal | View Issue

Cite this: *Nanoscale*, 2016, **8**, 10739

Open Access Article. Published on 18 April 2016. Downloaded on 18/10/2016 21:34:14. This article is licensed under a Creative Commons Attribution 3.0 Unported Licence.

Tunable top-down fabrication and functional surface coating of single-crystal titanium dioxide nanostructures and nanoparticles†

Seungkyu Ha, Richard Janissen, Yera Ye. Ussembayev, Maarten M. van Oene, Belen Solano and Nynke H. Dekker*

Received 1st February 2016, Accepted 17th April 2016

DOI: 10.1039/c6nr00898d

www.rsc.org/nanoscale

Titanium dioxide (TiO_2) is a key component of diverse optical and electronic applications that exploit its exceptional material properties. In particular, the use of TiO_2 in its single-crystalline phase can offer substantial advantages over its amorphous and polycrystalline phases for existing and yet-to-be-developed applications. However, the implementation of single-crystal TiO_2 has been hampered by challenges in its fabrication and subsequent surface functionalization. Here, we introduce a novel top-down approach that allows for batch fabrication of uniform high-aspect-ratio single-crystal TiO_2 nanostructures with targeted sidewall profiles. We complement our fabrication approach with a functionalization strategy that achieves dense, uniform, and area-selective coating with a variety of biomolecules. This allows us to fabricate single-crystal rutile TiO_2 nanocylinders tethered with individual DNA molecules for use as force- and torque-transducers in an optical torque wrench. These developments provide the means for increased exploitation of the superior material properties of single-crystal TiO_2 at the nanoscale.

Introduction

Micro- and nanostructures based on titanium dioxide (TiO_2) have been utilized in numerous applications that exploit the unique properties of this material (Fig. S1†). For example, the high photocatalytic activity of TiO_2 is used for water splitting[1] and air purification.[2] The electrical properties of TiO_2, which include a tunable resistance, a high dielectric constant, carrier transport abilities, and a wide band gap, render it a preferred material for sensors,[3] memory devices,[4] transistors,[5] solar cells,[6] and batteries.[7,8] Furthermore, the optical properties of TiO_2, *e.g.* high refractive index and optical nonlinearity, make it find use in optical waveguides,[9] photonic crystals,[10] and optical trapping.[11]

In particular, the use of TiO_2 in its single-crystalline phase can offer substantial advantages over its amorphous and polycrystalline phases for existing and new applications. For instance, single-crystal TiO_2 allows improved control of surface properties, *e.g.* photochemical reactivity[12] and surface wettability,[13] by making use of the different crystallographic orientations. The higher carrier mobility of single-crystal TiO_2 renders it a promising material for transistors and (bio)-sensors[14] and may enhance the efficiency of dye-sensitized solar cells.[15] Furthermore, optical waveguides and photonic crystals composed of single-crystal TiO_2 [16,17] are expected, due to their highly ordered atomic structures, to exhibit improved light transmission and nonlinear responses.[18,19] Lastly, the single-crystal rutile polymorph of TiO_2 has an exceptionally large optical birefringence, which makes it an excellent candidate for incorporation into torque transducers for *e.g.* single-molecule spectroscopy.[20]

To facilitate the application of TiO_2 in its single-crystalline phase, major challenges in both fabrication and surface functionalization must be addressed. First, it is important to control structural parameters such as feature size, shape, and pitch that determine the resulting physical responses of fabricated TiO_2 nanostructures. Such physical responses impact *e.g.* gas sensing performance,[3] light scattering efficiency,[6] light propagation behavior,[9] and optical trapping capabilities.[11]

Department of Bionanoscience, Kavli Institute of Nanoscience, Faculty of Applied Sciences, Delft University of Technology, Lorentzweg 1, 2628 CJ Delft, The Netherlands. E-mail: n.h.dekker@tudelft.nl

† Electronic supplementary information (ESI) available: Experimental details (ESI Methods) of the optic axis orientation of TiO_2 nanocylinders, Cr etch mask fabrication, surface functionalization and its evaluation using fluorescence microscopy, preparation of DNA constructs, assembly of flow cells, bioconjugation of TiO_2 nanocylinders, OTW instrumentation and measurements; TiO_2 dry etching optimization and the etching parameters employed (Tables S1 and S2); dimensional analysis of TiO_2 nanocylinders (Table S3); diverse applications of TiO_2 at the nanoscale (Fig. S1); selection of etch mask material (Fig. S2); control of sidewall profiles in TiO_2 etching (Fig. S3); size distributions of TiO_2 nanocylinders (Fig. S4); quantitative comparisons of different surface linker molecules (Fig. S5); DLS measurements on TiO_2 nanocylinders (Fig. S6); optical trap calibration (Fig. S7); and supplementary references. See DOI: 10.1039/c6nr00898d

This journal is © The Royal Society of Chemistry 2016

Open Access Article. Published on 18 April 2016. Downloaded on 18/10/2016 21:34:14.
This article is licensed under a Creative Commons Attribution 3.0 Unported Licence.

Mainstream bottom-up approaches for TiO_2 nanofabrication,[21] *e.g.* the hydrothermal growth method[1,22] and electrochemical anodization,[6] although capable of high throughput, lack sufficient flexibility in controlling dimensions and geometries. A number of bottom-up methods are capable of fabricating single-crystal TiO_2 nanostructures, but these lack control of the crystallographic orientations and are limited to a certain crystalline polymorph, *e.g.* anatase[23] or rutile.[15] Hybrid fabrication methods, such as the atomic layer deposition array defined by etch-back technique,[24,25] can achieve a high aspect-ratio but are limited to the fabrication of amorphous or poly-crystalline TiO_2.[26] These limitations can be overcome by employing top-down nanofabrication methods based on plasma etching, which can target a single-crystal TiO_2 substrate with any desired crystalline polymorph or crystallographic orientation. However, as TiO_2 is substantially more difficult to etch than comparable materials (*e.g.*, silicon (Si), silicon dioxide (SiO_2), and silicon nitride (Si_3N_4)),[27,28] such etching processes are currently limited to a low aspect-ratio and a largely positive sidewall angle.

Second, it is key to achieve highly efficient surface functionalization and bioconjugation of TiO_2 for applications such as (bio)sensors,[29] force transducers,[30] and torque transducers.[31] However, surface functionalization of TiO_2, using common alkoxysilane surface linkers, is known to be less efficient in terms of linker density and uniformity than other oxide materials (*e.g.*, SiO_2 and aluminum oxide (Al_2O_3)).[32,33] Furthermore, the majority of the described bioconjugation methods for TiO_2 surfaces require a long incubation time and additional crosslinker molecules[29] that could decrease the overall conjugation efficiency and harm the biomolecule functionality. Peculiarly for single-crystal TiO_2 nanostructures, the lack of extensive quantitative and qualitative comparisons of different surface functionalization strategies hinders the selection of an optimal procedure.

Here, we present a successful top-down fabrication and surface functionalization of single-crystal TiO_2 nanostructures and nanoparticles. We focus our efforts on the rutile polymorph of single-crystal TiO_2 (100), in order to harness its exceptionally large optical birefringence and precisely oriented optic axis for effective torque transfer (ESI Methods†) in an optical torque wrench (OTW).[20] Using high aspect-ratio nanocylinders suitable for optical trapping as our target structures, we demonstrate how these can be mass-produced with well-defined sizes and etch profiles that display excellent overall structural uniformity. We achieve a dense, uniform surface coating of TiO_2 nanocylinders using different linker molecules, and we demonstrate subsequent covalent conjugation of biological and organic molecules such as DNA, streptavidin, biotin, and biocompatible poly(ethylene glycol) (PEG). We successfully exploit these developments to fabricate and functionalize TiO_2 nanocylinders with single DNA molecules, and demonstrate full rotational control of individual nanocylinders in an OTW. This provides a particularly stringent test, as proper functioning of the OTW relies on both the correctly oriented optic axis and tightly controlled dimension of the single-crystal TiO_2 nanocylinder, and the quality and reliability of the surface coating. Rutile being the polymorph of TiO_2 that is most difficult to etch,[34] our approach provides the means for increased exploitation of the superior material properties of single-crystal TiO_2 in any desired polymorph for diverse applications.

Results and discussion

Selecting an etch mask for the plasma etching of single-crystal TiO_2

One of the major issues in top-down nanofabrication of single-crystal TiO_2 is its high etch resistance. Plasma generated by fluorine-based gases is capable of etching TiO_2 only under more aggressive etching conditions – in terms of plasma ion density and energy – than the ones employed for the dry etching of comparable materials *e.g.* Si, SiO_2, and Si_3N_4. The increased difficulty in etching TiO_2 compared to *e.g.* SiO_2 stems from differences in the volatility of their etch byproducts: whereas SiF_x is volatile, TiF_x is not.[27] The more aggressive physical etching conditions for TiO_2 necessitate careful selection of the etch mask material: while a typical polymer-based mask (*e.g.*, photoresist, electron beam (e-beam) resist, or polystyrene spheres) can provide sufficient etch selectivity (defined as the ratio of the substrate and mask etch rates) for *e.g.* SiO_2,[31] this is not the case for TiO_2. The low etch selectivity imposes a thicker mask for a target etch depth, which is challenging as the applicable mask thickness is always limited (ESI Methods†). Also, masks can suffer from excessive edge erosion during etching, which in turn reduces both feature sizes and the ability to perform anisotropic etching.[35]

To overcome these challenges, we have searched for a mask material for the dry etching of single-crystal TiO_2 that achieves sufficiently high etch selectivity to permit the fabrication of nanostructures in a wide range of dimensions and sidewall profiles. We have compared different mask materials (Fig. S2†), such as chromium (Cr),[36] tungsten (W), e-beam resist, and amorphous Si. We observe that in particular Cr provides a significantly higher etch selectivity in fluorine-based etching of rutile TiO_2 (up to ∼28 : 1 under specific etching conditions; an overview of etch selectivity values for different etching conditions can be found in Fig. S3†) than the other tested materials. We therefore select Cr as an appropriate etch mask material. To fabricate the Cr mask, we create circular apertures in a poly(methyl methacrylate) (PMMA) layer using e-beam lithography (Fig. 1, steps 1–3). The aperture diameters can be tuned within 100–600 nm by means of defocusing e-beam. Subsequent Cr deposition and the following lift-off define the mask (Fig. 1, steps 4 and 5).

Trifluoromethane (CHF_3)-based plasma etching of single-crystal TiO_2 nanocylinders

With the objective to maximize the etch rate with a sufficiently high etch selectivity (>10 : 1, in order to achieve etch depths up to 1–2 μm at the practical upper limit of Cr mask thickness, ∼150 nm; ESI Methods†) and to produce single-crystal TiO_2

This journal is © The Royal Society of Chemistry 2016

Open Access Article. Published on 18 April 2016. Downloaded on 18/10/2016 21:34:14.
This article is licensed under a Creative Commons Attribution 3.0 Unported Licence.

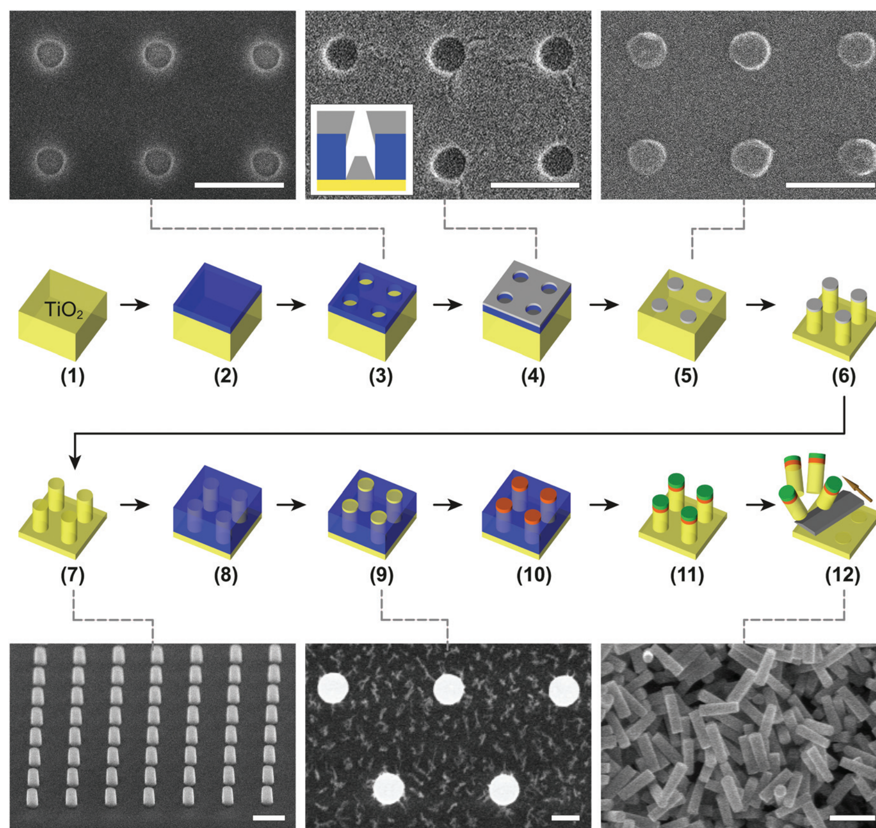

Fig. 1 Schematic diagram of the fabrication protocol for single-crystal TiO_2 nanostructures and nanoparticles. Each SEM image is linked to the corresponding step by a gray dashed line. Scale bars denote 500 nm. (Step 1) Cleaning of a single-crystal TiO_2 substrate (yellow). (Step 2) PMMA (blue) spin-coating for e-beam lithography. (Step 3) E-beam patterning and subsequent development to generate evaporation windows that define the desired nanostructure sizes. The corresponding SEM image in the inset shows the TiO_2 surfaces (circles) following exposure and development of the PMMA layer. (Step 4) Deposition of the Cr layer (light gray) through evaporation. The Cr layer covers both the accessible TiO_2 surfaces (circles) and the PMMA layer (inset SEM image). The inset illustration shows a cross-section that highlights the formation of a Cr mask. (Step 5) Lift-off of the PMMA layer and the resulting Cr etch mask. The SEM image in the inset displays the Cr mask (circles) formed on the TiO_2 substrate. (Step 6) Dry etching step to obtain the desired heights and sidewall profiles. (Step 7) Removal of the Cr mask following usage generates the complete nanostructures, and surface cleaning prepares these for subsequent surface functionalization. The SEM image (60° tilt) in the inset shows an array of the fabricated nanocylinders. (Step 8) Spin-coating of a temporary PMMA layer for area-selective functionalization. (Step 9) Etching of the temporary PMMA layer renders the tops of the nanostructures accessible. The SEM image in the inset shows the TiO_2 nanostructures (white circles) amidst the etched PMMA layer. (Step 10) Selective surface functionalization with linker molecules (orange). (Step 11) Removal of the temporary PMMA layer and the following conjugation with biomolecules (green). (Step 12) Mechanical cleavage of the nanostructures using a microtome blade (dark gray) to generate isolated individual nanoparticles. The inset shows an SEM image of a batch of cleaved nanocylinders. For further details, see Methods.

nanocylinders with vertical sidewall angles, we have optimized parameters for the fluorine-based plasma etching process (Fig. 1, step 6). We start with a reactive ion etching (RIE) system in which trifluoromethane (CHF_3) is the major etchant, and oxygen (O_2) and argon (Ar) are additive gases. The major etchant gas CHF_3 supplies both the reactive etching species and the fluorocarbon (C_xF_y) surface passivation layer-forming species.[37] To optimize the process, we systematically vary the radio frequency (RF) power, chamber pressure, and ratios of the etch gases ($CHF_3 : O_2 : Ar$) (Table S1†). Our optimized etching conditions (Table S2†) result in a high single-crystal TiO_2 etch rate of ~40 nm min^{-1} at a sufficient etch selectivity of ~14 : 1 over the Cr mask, which enables the formation of TiO_2 nanocylinders with vertical sidewalls (~90°; Fig. 2a). We have successfully implemented this protocol on a second, nominally identical RIE system (Fig. 2b), requiring only minor tuning in the O_2 flow rate (4–8 sccm compared to ~0.5 sccm), most likely due to differences in instrument calibration.

Notably, we observe that tuning a single process parameter, namely the O_2 flow rate, allows us to drastically alter sidewall etch profiles and even cross-sectional shapes (Fig. S3†). For example, at low O_2 flow rates (0–1 sccm), we can modulate the sidewall angles from positive to negative, thereby including vertical sidewalls (Fig. 2a and b). At significantly higher O_2 flow rates (5–10 sccm), we can obtain hourglass-shaped etch profiles (Fig. 2c).

Sulfur hexafluoride (SF_6)-based plasma etching of single-crystal TiO_2 nanocylinders

While maintaining identical objectives as above (high etch selectivity and vertical sidewall angles), we have also optimized the plasma etching of TiO_2 using another major etchant,

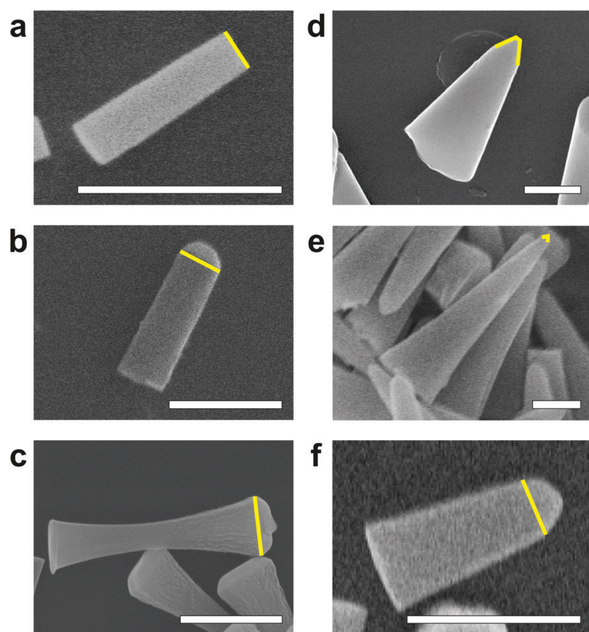

Fig. 2 Control of single-crystal TiO_2 nanocylinder shapes using different conditions in plasma etching. In each SEM image, the top surface of the nanocylinder is marked by a yellow line (remnants of the Cr mask prior to its removal are visible in (b, c and f)). Scale bars denote 500 nm. In the following, the height (*H*), the averaged diameter (*D*), and the resulting aspect-ratio (AR = *H*/*D*) of each nanocylinder are shown. (a) A nanocylinder with a vertical sidewall (89°) that results from an optimized $CHF_3:O_2$ dry etching in an RIE system (*H*: 430 nm, *D*: 110 nm, AR: 3.9). (b) A nanocylinder with a vertical sidewall (89°) etched from the optimized $CHF_3:O_2$ dry etching in a second, nominally identical RIE system (*H*: 605 nm, *D*: 205 nm, AR: 3.0). (c) An hourglass-shaped nanocylinder that results from $CHF_3:O_2:Ar$ dry etching in an RIE system (*H*: 1020 nm, *D*: 200 nm, AR: 5.1). (d) A cone-shaped nanocylinder that results from $SF_6:CH_4:Ar$ dry etching in an ICP-RIE system (*H*: 1385 nm, *D*: 490 nm, AR: 2.8). (e) A cone-shaped nanocylinder that results from $SF_6:He$ dry etching in an ICP-RIE system (*H*: 2160 nm, *D*: 390 nm, AR: 5.5). (f) A nearly vertical (85°) nanocylinder that results from an optimized $SF_6:He$ dry etching in an ICP-RIE system (*H*: 470 nm, *D*: 210 nm, AR: 2.2).

Open Access Article. Published on 18 April 2016. Downloaded on 18/10/2016 21:34:14.
This article is licensed under a Creative Commons Attribution 3.0 Unported Licence.

sulfur hexafluoride (SF_6), in inductively coupled plasma (ICP)-RIE systems. We achieve higher etch rates of 100–200 nm min^{-1} (compared to those of 30–100 nm min^{-1} in RIE systems) using two different ICP-RIE systems (one equipped with SF_6, methane (CH_4), and Ar gases, Fig. 2d; the other equipped with SF_6 and helium (He) gases, Fig. 2e and f), making it possible to fabricate TiO_2 nanocylinders with heights up to 1–2 μm while reducing the time of exposure to the plasma. The latter is important because longer etch durations tend to induce a drift in the etching conditions which in turn leads to irregular etch profiles. The higher TiO_2 etch rates that we obtain result from the increased density of plasma generated in ICP-RIE *versus* RIE systems[28] and a reduced level of C_xF_y sidewall surface passivation. Decreased levels of C_xF_y passivation are attributed to an excess of hydrogen plasma[38] and to the lack of a carbon source for the cases of $SF_6:CH_4:Ar$ and $SF_6:He$, respectively. Furthermore, SF_6-etched nanocylinders show cleaner, smoother surfaces in high-resolution scanning electron microscopy (SEM) images (Fig. 2d) compared to those of CHF_3-etched cylinders (Fig. 2c).

When we use non-optimized SF_6-based plasma etching conditions, etch profiles displaying highly positive sidewall angles are obtained. Since the high plasma densities of ICP-RIE systems also significantly increase the Cr etch rates, we observe that the Cr mask tends to be completely etched away during the process, hence resulting in the formation of cone-shaped nanocylinders[35] (Fig. 2d and e). Under our optimized etching conditions (Table S2†), which rely on a reduced ICP power to generate moderate plasma density, we are able to achieve sufficient etch selectivity over the Cr mask (∼16 : 1) and nearly vertical sidewall angles (∼85°; Fig. 2f) with high single-crystal TiO_2 etch rates of ∼120 nm min^{-1}.

Quantification of single-crystal TiO_2 nanocylinder uniformity

To quantify both the local and global structural uniformity of fabricated single-crystal TiO_2 nanocylinders over an entire substrate, we have analyzed SEM images of high aspect-ratio (3.6) nanocylinders fabricated using the CHF_3 plasma-based protocol (Fig. 3; etching conditions in Table S2†). Qualitatively, the high uniformity of nanocylinder diameters and heights can be observed from the SEM image of a cleaved nanocylinder substrate (Fig. 3a). To quantify this, we measure the dimensions of nanocylinders at radial distances from the substrate center out to 3.5 mm and spaced by 0.5 mm (thus covering the entire circularly patterned area with a radius of ∼4 mm on the 10 × 10 mm^2-sized substrate). From the analysis of top-view SEM images (Fig. 3b), we observe that the top (Fig. 3d) and bottom diameters (Fig. 3e) exhibit excellent local uniformity, defined as the uniformity at each measurement position (averaged relative standard deviation (RSD) of 4.4% (top) and 2.3% (bottom)). The global uniformity across the substrate displayed similar values (RSD of 4.7% (top) and 2.7% (bottom)). Fluctuations in diameters likely result from the instability of the e-beam during the patterning process of the Cr etch mask. The observation that the top diameters are nonetheless slightly less uniform than the bottom diameters may result from the fact that etching erodes the Cr mask in a non-uniform fashion depending on the roughness of the mask surface,[39] as is backed up by an analysis of the roundness of the top and bottom nanocylinder surfaces (Fig. S4†). From tilted-view SEM images (Fig. 3c), we also extract the nanocylinder heights (Fig. 3f), which similarly show very good uniformity both locally (averaged RSD of 0.6%) and globally (RSD of 1.4%). We attribute the nearly monotonic increase in heights outward from the substrate center to the well-known loading effect, in which the transport and depletion of etching species along a substrate contribute to etch rate nonuniformity.[40] The analysis of a batch of low aspect-ratio (1.6) nanocylinders reveals identical trends (Fig. S4 and Table S3;† etching conditions in Table S2†), thereby proving that our protocol can be used to generate both low and high aspect-ratio nanoscale structures with high uniformity.

This journal is © The Royal Society of Chemistry 2016

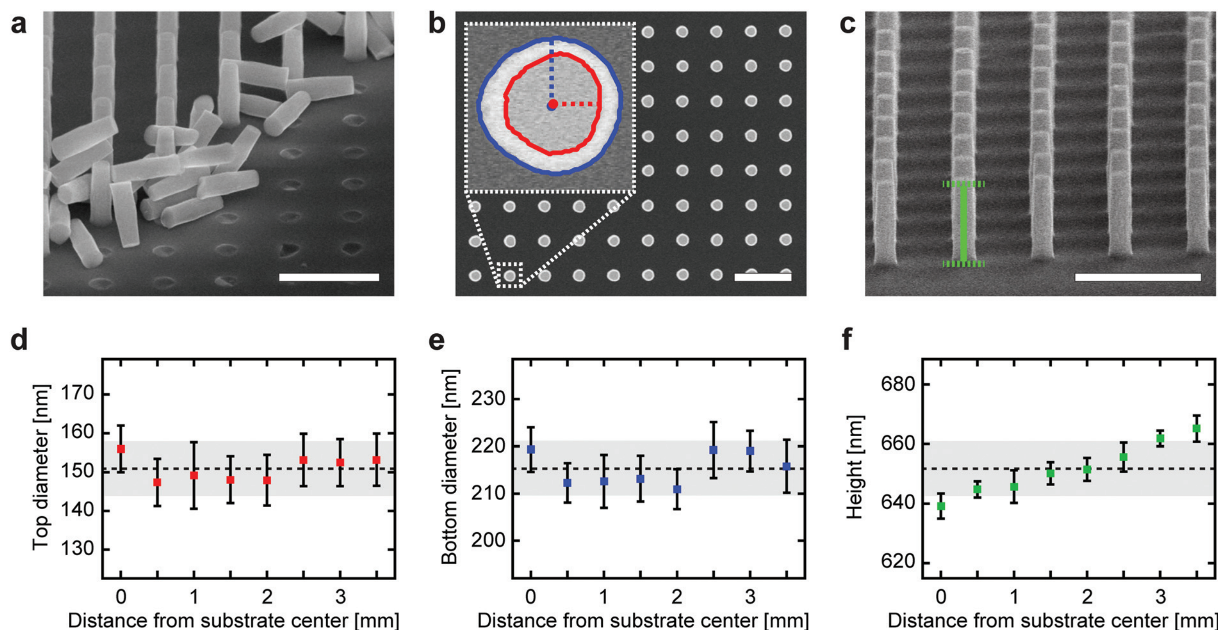

Fig. 3 Dimensions of fabricated single-crystal TiO_2 nanocylinders. (a–c) SEM images of etched TiO_2 nanocylinders (light gray). Scale bars denote 1 µm. (a) Tilted-view (60°) of partially cleaved TiO_2 nanocylinders. An array of rigidly fixed nanocylinders is visible in the top-left corner, and the cleaved substrate surface is in the bottom-right corner. The released nanocylinders are positioned at the interface of these regions. (b) Top-view of the nanocylinders. The inset shows the boundaries of the top (red contour line) and bottom (blue contour line) surface areas detected using the custom-written image analysis software routine. The dotted horizontal red (vertical blue) line and the red (blue) dot display the equivalent radius and the center of the top (bottom) surface, respectively. (c) Tilted-view (75°) together with an illustration of the image analysis procedure used to extract nanocylinder heights. The green vertical line measures the distance between the centers of the top and bottom surfaces (indicated by the green dotted horizontal lines). This distance is converted to the actual height using the tilting angle. (d–f) Quantification of nanocylinder diameters and heights over the substrate. Measurement points are spaced by 0.5 mm from the center of the substrate to its edge. At each point, the diameters (heights) are calculated from n = 12 (n = 10) different nanocylinders. The square markers and the error bars in the graphs represent the mean and the standard deviation of the local uniformity, respectively. The horizontal dotted black lines and the top and bottom sides of the gray shaded boxes in the graphs represent the mean and the standard deviation of the global uniformity, respectively. (d) Top diameters, (e) bottom diameters, and (f) heights are shown as a function of distance from the substrate center.

Open Access Article. Published on 18 April 2016. Downloaded on 18/10/2016 21:34:14.
This article is licensed under a Creative Commons Attribution 3.0 Unported Licence.

Surface functionalization and bioconjugation of single-crystal TiO_2

We now demonstrate highly efficient and versatile surface functionalization and bioconjugation of single-crystal rutile TiO_2 (Fig. 4a). We perform the functionalization experiments on single-crystal TiO_2 nanostructures fabricated using our developed SF_6-based plasma etching process presented earlier. Compared with CHF_3-based etching, this process results in a lower degree of surface contamination by C_xF_y, and hence a higher surface linker coverage.

To quantitatively characterize the surface coating efficiency of different covalently bound surface linkers, we first test functionalization on single-crystal rutile TiO_2 substrates with large-scale square micro-patterns (25 × 25 µm^2) embedded in a thick (1–2 µm) PMMA layer (Fig. 4b). Similarly to other oxide materials, the surface of TiO_2 is populated by hydroxyl groups that allow it to be functionalized with different types of linker molecules, such as silanes and other organic molecules with a covalent hydroxyl-binding capacity.[33,41] Here, we have tested four different surface linker molecules: an aminoalcohol (ethanolamine hydrochloride; ETA), an epoxysilane ((3-glycidoxypropyl)dimethylethoxysilane; GPDMES), a widely used alkoxysilane ((3-aminopropyl)dimethylethoxysilane; APDMES), and a cyclic azasilane (*N*-*n*-butyl-aza-2,2-dimethoxysilacyclopentane; BADMSCP). Additionally, since PEG coatings are widely used for surface passivation[42] and as biocompatibility layers,[43] we have also tested the covalent attachment of heterobifunctional PEG to ETA-coated surfaces (ESI Methods, Fig. S5†). To compare the coating efficiency of these different linkers, we covalently bind fluorophores (ATTO 647N; $\lambda_{excitation}$ = 640 nm, $\lambda_{emission}$ = 669 nm) to the functionalized micropatterns and measure the fluorescence intensity using quantitative fluorescence microscopy (ESI Methods†). The fluorescence measurements report successful surface functionalization for all the surface linkers used (Fig. S5†).

Regarding subsequent bioconjugation to TiO_2 surfaces, several considerations led us to select epoxysilane (GPDMES) as the most appropriate surface linker. To start, epoxysilanes are widely used for their demonstrated reliability in surface functionalization[44] and biomolecule attachment.[45] Furthermore, GPDMES-coated TiO_2 surfaces demonstrate high surface linker coating density and homogeneity (Fig. 4b). Indeed, while GPDMES coatings provide a slightly lower surface linker

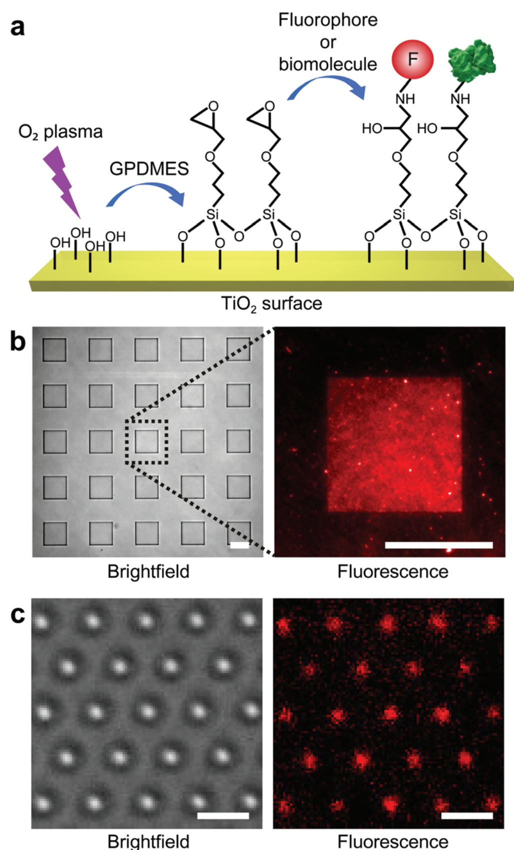

Fig. 4 Characterization of the efficiency of surface functionalization of single-crystal TiO_2 structures using fluorescence microscopy. (a) Illustration of the surface coating steps. First, single-crystal TiO_2 surfaces are O_2 plasma-treated to generate hydroxyl groups (–OH). Then epoxysilanes (GPDMES) are covalently bound to the surface hydroxyl groups. Consequently, either fluorophores (red) or biomolecules (*e.g.*, streptavidin (green)) are bound covalently to the reactive epoxy functional group. (b) Functionalized micro-patterns for the quantitative characterization of the efficiency of surface functionalization. The brightfield image (left panel) shows squares (25 × 25 μm^2) patterned on the PMMA-coated TiO_2 substrate. The corresponding zoom-in fluorescence image (right panel) of a square shows successful covalent binding of the amino-labeled fluorophores (ATTO 647N) to the epoxysilane functionalized surface. Scale bars denote 20 µm. (c) Functionalized nanostructures for the qualitative characterization of the efficiency of surface functionalization. Brightfield (left panel) and the corresponding fluorescence (right panel) images of top-area functionalized TiO_2 nanocylinders using the same method as above. Scale bars denote 2 µm.

Open Access Article. Published on 18 April 2016. Downloaded on 18/10/2016 21:34:14.
This article is licensed under a Creative Commons Attribution 3.0 Unported Licence.

density than ETA or PEGylated ETA coatings, their coating efficiency is significantly higher than the one obtained using BADMSCP and comparable to that of commonly used APDMES (Fig. S5†).

More importantly, the greatest advantages of using GPDMES compared to other surface linkers are: first, the ability of the epoxy group to react directly with the primary amino groups of biomolecules that permits bioconjugation in the absence of additional crosslinkers, avoiding conditions that could harm the structural and functional integrity of the target biomolecules; and second, the rapid surface functionalization process (*e.g.*, ∼15 min compared to ∼12 h of all the other linkers; ESI Methods†). With this procedure in hand, epoxysilane-functionalized TiO_2 surfaces can be readily used for the covalent conjugation of a majority of biomolecules. We apply this bioconjugation process to the single-crystal TiO_2 nanocylinder arrays on the substrate (Fig. 1, steps 7–11) prior to their mechanical cleaving (Fig. 1, step 12) to avoid additional, subsequent purification procedures. At this stage, functionalization can be applied to specific areas of the TiO_2 nanocylinders through partial PMMA coating (Fig. 1, steps 8–10). Using this approach, we are able to functionalize and bioconjugate only the top parts of the TiO_2 nanocylinders (Fig. 1, step 11). Fluorescence microscopy has also been used to qualitatively demonstrate the successful functionalization of individual TiO_2 nanocylinders (Fig. 4c).

Degree of monodispersity in coated single-crystal TiO_2 nanoparticles

Our ability to functionalize single-crystal TiO_2 nanoparticles with high surface linker density and homogeneity can also be beneficial in different contexts. For example, following the mechanical cleaving that liberates the nanocylinders from the TiO_2 substrate, it is necessary to prevent their aggregation in aqueous environments. Generally speaking, the aggregation of nanoparticles depends on both the surface composition of the nanoparticles and the type of solution in which they are immersed.[46] We have tested different surface coatings and buffer solutions that effectively prohibit single-crystal TiO_2 nanoparticle aggregation and have evaluated these using dynamic light scattering (DLS) measurements (Fig. S6†). We found that non-coated TiO_2 nanocylinders aggregate substantially over time in deionized (DI) water, in contrast to what occurs in physiological phosphate buffered saline (PBS) solution at a similar pH (7.4). We also found that the addition of bovine serum albumin (BSA, 2% (m/v)), which is widely used as a surface passivation agent,[47] deteriorates substantially the monodispersity of TiO_2 nanocylinders in both DI water and PBS solution. When we apply a PEG coating – widely implemented for passivating nanoparticle surfaces to decrease aggregation and for enhancing their biocompatibility[43] – to TiO_2 nanocylinders, we observe no aggregation in either DI water or PBS solution. Such PEG-coated TiO_2 nanocylinders refrain from aggregation even when they are conjugated to biomolecules such as biotin or DNA. Likewise, the GPDMES-coated TiO_2 nanocylinders with bioconjugated streptavidin show no aggregation under physiological conditions (PBS solution) and therefore have been chosen for the single-molecule OTW experiments.

Characterization of individual DNA molecules using single-crystal TiO_2 nanocylinders

To demonstrate the potential of our developed fabrication and surface coating processes for diverse applications, we tether single-crystal TiO_2 nanocylinders to individual linear, double-stranded DNA molecules and perform stretching and twisting experiments in an OTW. For these measurements, we use

This journal is © The Royal Society of Chemistry 2016

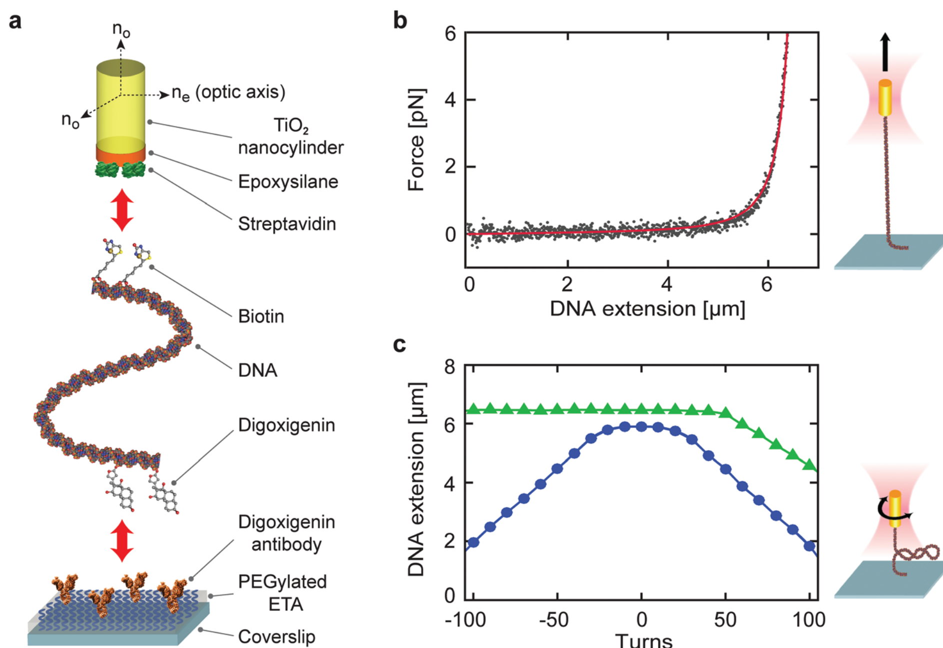

Fig. 5 Application of DNA-tethered single-crystal rutile TiO_2 nanocylinders in an OTW. (a) Schematic of a DNA tethered at one extremity to a single-crystal rutile TiO_2 nanocylinder and at the other extremity to a flow cell channel surface. For the nanocylinder, the orientations of ordinary (n_o) and extraordinary (n_e) refractive indices are indicated. First, we functionalize the flow cell channel surface with ETA, PEG, and digoxigenin antibodies. Then the end of the DNA containing the digoxigenin-enriched handle is attached to the flow cell channel surface *via* antigen–antibody binding. The other extremity of the DNA that contains the biotin-enriched handle binds to the streptavidin-coated nanocylinder. (b) The extension of tethered DNA as a function of force. The gray dots represent force-extension data while the red line is a fit to the WLC model. The illustration depicts a fully stretched DNA. (c) The response of DNA to rotation at different stretching forces (blue circles and green triangles for 0.5 pN and 1.8 pN, respectively). The corresponding illustration represents a supercoiled DNA.

Open Access Article. Published on 18 April 2016. Downloaded on 18/10/2016 21:34:14.
This article is licensed under a Creative Commons Attribution 3.0 Unported Licence.

GPDMES-functionalized, streptavidin-coated single-crystal TiO_2 nanocylinders fabricated in SF_6 plasma (Methods), and test their response to force and torque applied on torsionally constrained 20.6 kbp DNA (contour length of ~7 μm; ESI Methods†). A biotinylated handle on one extremity of the DNA is designed to bind to the streptavidin-coated nanocylinders, whereas the other extremity of the DNA includes digoxigenin to allow it to bind to the digoxigenin antibodies that are covalently bound to a heterobifunctional PEG-coated flow cell channel (Fig. 5a, ESI Methods†).

Prior to performing measurements on these DNA-tethered single-crystal TiO_2 nanocylinders in an OTW (ESI Methods†), we calibrate the optical trap by using individual non-tethered nanocylinders to measure its trap stiffness (Fig. S7†). We can then apply a force to a tethered nanocylinder and stretch the DNA (Fig. 5b). The obtained force-extension data are fitted to the worm-like chain (WLC) model[48] (red line in Fig. 5b) and yield a persistence length of 45 ± 1 nm and a contour length of 6.8 ± 0.2 μm (means and standard deviations for n = 5 different DNA tethers), in excellent agreement with previous reports.[30,31,48] We additionally rotate the nanocylinder at low constant force (0.5 pN) or medium constant force (1.8 pN) to supercoil the tethered DNA molecule. The resulting extension–rotation relationship (Fig. 5c) shows the characteristic symmetric (asymmetric) response of twisted DNA in the low (medium) force regime, also in agreement with previous reports.[31,49–52] We note that the OTW provides an excellent platform to evaluate the quality of our top-down fabrication of single-crystal TiO_2 nanostructures, as only nanocylinders with precisely controlled dimensions and uniformity are appropriate for stable and reproducible optical trapping. Furthermore, the use of the OTW to stretch and twist DNA molecules provides a stringent test of the applied surface functionalization, as these processes (notably twisting) are only possible provided that the surface functionalization and bioconjugation processes are sufficiently efficient to allow for the formation of multiple stable bonds at either DNA extremity.[52]

Conclusions

We have developed and optimized processes for the fabrication, surface functionalization, and bioconjugation of single-crystal TiO_2 nanostructures and nanoparticles. Using two top-down etching approaches, we demonstrate the fabrication of highly uniform nanostructures and nanoparticles with controllable shapes and dimensions. The CHF_3-based etching process provides a wider range of etch geometries, while the SF_6-based etching process results in improved surface quality allowing homogeneous and dense coating. We are able to etch single-crystal TiO_2 into various nanoscale shapes, including cylinders, cones, and hourglass-shaped structures. The fabricated

nanostructures have diameters in the range of 100–600 nm, with heights up to 1–2 μm under etching conditions that yield high etch rate and selectivity. Using SF_6-etched single-crystal TiO_2 nanocylinders, we show how they can be functionalized with high efficiency and be conjugated covalently to a majority of biomolecules. We demonstrate the use of these coated TiO_2 nanocylinders by stretching and twisting individually tethered DNA molecules, an application that exploits the tight dimensional control and high quality surface functionalization of nanocylinders etched from a rutile (100) single-crystal TiO_2 substrate. Our developed fabrication and surface functionalization methods will likely find utilization in diverse optical and electronic applications of single-crystal TiO_2, including applications in life science-oriented fields through *e.g.* the development of biosensors and single-molecule techniques.

Open Access Article. Published on 18 April 2016. Downloaded on 18/10/2016 21:34:14. This article is licensed under a Creative Commons Attribution 3.0 Unported Licence.

Methods

Fabrication and bioconjugation of single-crystal rutile TiO_2 nanocylinders for OTW experiments

We use single-side polished single-crystal rutile TiO_2 (100) substrates (Latech, Singapore), 10 × 10 mm^2 in size and 0.5 mm in thickness, to produce nanocylinders. We clean the substrates in fuming nitric acid (99.5%, Sigma-Aldrich, The Netherlands) using ultrasonication for 10 min followed by thorough rinsing in DI water and drying under a nitrogen (N_2) stream (Fig. 1, step 1). We then subject the substrates to an O_2 plasma (TePla300, PVA TePla, Germany), after which we spin-coat a ~250 nm-thick e-beam resist layer (PMMA 950k A4, MicroChem, Germany) at 500 rpm for 5 s and then 3000 rpm for 55 s. We bake the resist-coated substrates on a hotplate for 30 min at 175 °C (Fig. 1, step 2). The substrates do not require an additional conductive layer to prevent charge accumulation during e-beam patterning since it has sufficiently high electrical conductivity.

We then use an e-beam patterning system (EBPG 5000+, Leica, UK; the acceleration voltage is set to 100 kV and the aperture diameter to 400 μm) to pattern the PMMA layer by a defocused e-beam with circular cross-section and tunable diameter. The patterning of each circular shape is performed by a single-pixel e-beam exposure, defining the shapes of the Cr mask for subsequent nanocylinder etching. Using optimized e-beam conditions (a current of 85 nA, a defocusing of 100–200 nm, and a dose of 2000 $\mu C\ cm^{-2}$), we pattern circles with 600 nm pitch on a circular patterning area with radius ~4 mm (~140 million masks in total) in <30 min. We develop the patterned substrate using a solution of methyl isobutyl ketone (MIBK, Sigma-Aldrich, The Netherlands) and isopropyl alcohol (IPA, Sigma-Aldrich, The Netherlands) (1 : 3 MIBK : IPA) for 60 s with constant hand agitation at room temperature. We then rinse the substrate in IPA for 30 s and dry it under a N_2 stream (Fig. 1, step 3).

We deposit the Cr mask layer using either an e-beam evaporator (Temescal FC-2000, Ferrotec, Germany) or a thermal evaporator (L560, Leybold Heraeus, Germany) loaded with Cr pieces (purity of 99.95%, Kurt J. Lesker, Germany), using the patterned PMMA layer as evaporation windows. We use slow Cr deposition rates (≤1.0 Å s^{-1}) to obtain high quality Cr layers (Fig. 1, step 4). We finalize Cr mask formation in a lift-off process by soaking the substrate into a preheated (80 °C) resist stripper (PRS-3000, JTBaker, The Netherlands) for 20 min with constant agitation using a magnetic spinner. Then we thoroughly rinse the substrate in DI water and dry it under a N_2 stream (Fig. 1, step 5).

We etch TiO_2 nanocylinders using the optimized conditions (Table S2†) for vertical sidewall angles (Fig. 1, step 6). We etch nanocylinders with either an RIE system (Fluor Z401S, Leybold Heraeus, Germany; Fig. 2a and b) or an ICP-RIE system (Plasmalab system 100, Oxford Instr., UK; Fig. 2f). For dimensional analysis of the etched nanocylinders, we employ SEM systems (Hitachi S4800 FESEM, FEI XL30S FEG SEM, or FEI Nova NanoSEM). We remove the used Cr mask using a wet etchant (Chromium Etchant N° 1, MicroChemicals, Germany) and then perform surface cleaning using fuming nitric acid and O_2 plasma (TePla300) for the subsequent surface functionalization (Fig. 1, step 7).

Optionally, if area-selective functionalization on top of the nanocylinders is required, we cover their sidewalls with a temporary protection layer. We cover the substrate with a PMMA 950k resist at a chosen concentration to provide a spin-coated thickness larger than the heights of the nanocylinders (Fig. 1, step 8). Consequently, we etch the PMMA layer to render the tops of the nanocylinders accessible, using either O_2 plasma (TePla300) or a MIBK solution (Fig. 1, step 9). Note that we do not bake the resist in order to allow for its straightforward removal afterwards.

To attach biomolecules to TiO_2 nanocylinders, we first activate the nanocylinder substrates by O_2 plasma treatment (Plasma-PREEN I, Plasmatic Systems Inc., USA). Then we bind GPDMES to the substrate for 15 min at 75 °C using non-diluted GPDMES solution, and wash the substrate in chloroform (CHROMASOLV plus, for HPLC, ≥99.9%, Sigma-Aldrich, The Netherlands) three times for 15 s each, followed by drying under a N_2 stream (Fig. 1, step 10). (If a temporary PMMA layer is used for area-selective functionalization, we first wash the substrate in ethanol three times for 15 s each directly after the incubation with GPDMES, followed by drying under a N_2 stream. We then remove the temporary PMMA layer in chloroform for 15 min at room temperature, followed by an additional washing in fresh chloroform three times for 15 s each and drying under a N_2 stream.)

We then bind streptavidin molecules to the epoxy group of GPDMES by incubating the nanocylinders with 2 μM streptavidin (Sigma-Aldrich, The Netherlands) in PBS solution (pH 7.4, Sigma-Aldrich, The Netherlands) for 1 h at room temperature. After washing the substrate three times for 15 s each with PBS/TWEEN® solution (pH 7.4, PBS containing 0.1% (v/v) TWEEN® 20 (Sigma-Aldrich, The Netherlands)), we wash the substrate with PBS solution (pH 7.4) another three times for 15 s each (Fig. 1, step 11).

We cleave TiO_2 nanocylinders mechanically from the substrate using a diamond microtome blade (DT315D50, C.L.

 This journal is © The Royal Society of Chemistry 2016

Sturkey, USA) inside a PBS/Triton™ droplet (pH 7.4, PBS containing 0.05% (v/v) Triton™ X-100 (Sigma-Aldrich, The Netherlands)), followed by suction of the droplet using a micropipette (Fig. 1, step 12). These cleaved, streptavidin-coated TiO_2 nanocylinders can be further coupled with biomolecules of interest, *e.g.* DNA with biotinylated handles, by incubating them in a flow cell channel for OTW experiments (ESI Methods†).

Open Access Article. Published on 18 April 2016. Downloaded on 18/10/2016 21:34:14.
This article is licensed under a Creative Commons Attribution 3.0 Unported Licence.

Acknowledgements

We acknowledge Z. Huang for his initial help in TiO_2 fabrication and M. Zuiddam, C. de Boer, M. van der Krogt, A. van Run, A. van Langen-Suurling, H. Miro, R. Mattern, Y. Caspi, and M. Jonsson for helpful discussions and advice on fabrication steps. We also thank T. van Laar for the preparation of DNA constructs, J. Kerssemakers, M. Docter, and V. M. Lizarraga for helpful discussions on the OTW setup, M. Ganji and O. Ordu for support in testing the surface functionalization protocol, J. van der Does and D. de Roos for the production of custom-made mechanical parts for the OTW setup and nanocylinder-cleaving tools, S. Khaiboulov for his help with laboratory infrastructure, and B. A. Berghuis and S. Pud for reviewing the manuscript. This research is supported by NanoNextNL, a micro and nanotechnology consortium of the Government of the Netherlands and 130 partners, and the Foundation for Fundamental Research on Matter (FOM), which is part of the Netherlands Organisation for Scientific Research (NWO), and by the European Research Council (ERC) *via* the DynGenome project (N° 312221).

References

1 G. Wang, H. Wang, Y. Ling, Y. Tang, X. Yang, R. C. Fitzmorris, C. Wang, J. Z. Zhang and Y. Li, *Nano Lett.*, 2011, **11**, 3026–3033.
2 H. Yu, K. Zhang and C. Rossi, *Indoor Built Environ.*, 2007, **16**, 529–537.
3 S. Hwang, H. Kwon, S. Chhajed, J. W. Byon, J. M. Baik, J. Im, S. H. Oh, H. W. Jang, S. J. Yoon and J. K. Kim, *Analyst*, 2013, **138**, 443–450.
4 E. Gale, *Semicond. Sci. Technol.*, 2014, **29**, 104004.
5 W. S. Shih, S. J. Young, L. W. Ji, W. Water and H. W. Shiu, *J. Electrochem. Soc.*, 2011, **158**, H609–H611.
6 X. Liu, M. Guo, J. Cao, J. Lin, Y. H. Tsang, X. Chen and H. Huang, *Nanoscale Res. Lett.*, 2014, **9**, 1–5.
7 Y. Tang, Y. Zhang, J. Deng, D. Qi, W. R. Leow, J. Wei, S. Yin, Z. Dong, R. Yazami, Z. Chen and X. Chen, *Angew. Chem., Int. Ed.*, 2014, **53**, 13488–13492.
8 Y. Tang, Y. Zhang, X. Rui, D. Qi, Y. Luo, W. R. Leow, S. Chen, J. Guo, J. Wei, W. Li, J. Deng, Y. Lai, B. Ma and X. Chen, *Adv. Mater.*, 2016, **28**, 1567–1576.
9 J. D. B. Bradley, C. C. Evans, J. T. Choy, O. Reshef, P. B. Deotare, F. Parsy, K. C. Phillips, M. Lončar and E. Mazur, *Opt. Express*, 2012, **20**, 23821–23831.
10 X. Wang, M. Fujimaki and K. Awazu, *Opt. Express*, 2005, **13**, 1486–1497.
11 A. Jannasch, A. F. Demirors, P. D. J. van Oostrum, A. van Blaaderen and E. Schäffer, *Nat. Photonics*, 2012, **6**, 469–473.
12 P. A. Morris Hotsenpiller, J. D. Bolt, W. E. Farneth, J. B. Lowekamp and G. S. Rohrer, *J. Phys. Chem. B*, 1998, **102**, 3216–3226.
13 R. Wang, N. Sakai, A. Fujishima, T. Watanabe and K. Hashimoto, *J. Phys. Chem. B*, 1999, **103**, 2188–2194.
14 J. M. Baik, M. H. Kim, C. Larson, X. Chen, S. Guo, A. M. Wodtke and M. Moskovits, *Appl. Phys. Lett.*, 2008, **92**, 242111.
15 X. Feng, K. Zhu, A. J. Frank, C. A. Grimes and T. E. Mallouk, *Angew. Chem.*, 2012, **124**, 2781–2784.
16 Z.-F. Bi, L. Wang, X.-H. Liu, S.-M. Zhang, M.-M. Dong, Q.-Z. Zhao, X.-L. Wu and K.-M. Wang, *Opt. Express*, 2012, **20**, 6712–6719.
17 K. Awazu, M. Fujimaki, Y. Ohki and T. Komatsubara, *Radiat. Meas.*, 2005, **40**, 722–729.
18 A. M. Agarwal, L. Liao, J. S. Foresi, M. R. Black, X. Duan and L. C. Kimerling, *J. Appl. Phys.*, 1996, **80**, 6120–6123.
19 A. Stone, H. Jain, V. Dierolf, M. Sakakura, Y. Shimotsuma, K. Miura, K. Hirao, J. Lapointe and R. Kashyap, *Sci. Rep.*, 2015, **5**, 10391.
20 J. Lipfert, M. M. van Oene, M. Lee, F. Pedaci and N. H. Dekker, *Chem. Rev.*, 2015, **115**, 1449–1474.
21 Y. Wang, Y. He, Q. Lai and M. Fan, *J. Environ. Sci.*, 2014, **26**, 2139–2177.
22 Y. Tang, Y. Zhang, J. Deng, J. Wei, H. Le Tam, B. K. Chandran, Z. Dong, Z. Chen and X. Chen, *Adv. Mater.*, 2014, **26**, 6111–6118.
23 Z. Miao, D. Xu, J. Ouyang, G. Guo, X. Zhao and Y. Tang, *Nano Lett.*, 2002, **2**, 717–720.
24 Y. Huang, G. Pandraud and P. M. Sarro, *Nanotechnology*, 2012, **23**, 485306.
25 E. Shkondin, J. Michael-Lindhard, M. D. Mar, F. Jensen and A. Lavrinenko, presented in part at the 15th Int'l Conf. on Atomic Layer Deposition, Portland, United States, June 2015.
26 H. Y. Jeong, J. Y. Lee and S.-Y. Choi, *Appl. Phys. Lett.*, 2010, **97**, 42109.
27 J. Dekker, K. Kolari and R. L. Puurunen, *J. Vac. Sci. Technol., B*, 2006, **24**, 2350–2355.
28 F. Karouta, *J. Phys. D: Appl. Phys.*, 2014, **47**, 233501.
29 J. Tang, Y. Wang, J. Li, P. Da, J. Geng and G. Zheng, *J. Mater. Chem. A*, 2014, **2**, 6153–6157.
30 M. D. Wang, H. Yin, R. Landick, J. Gelles and S. M. Block, *Biophys. J.*, 1997, **72**, 1335–1346.
31 Z. Huang, F. Pedaci, M. Van Oene, M. J. Wiggin and N. H. Dekker, *ACS Nano*, 2011, **5**, 1418–1427.
32 S. P. Pujari, L. Scheres, A. T. M. Marcelis and H. Zuilhof, *Angew. Chem., Int. Ed.*, 2014, **53**, 6322–6356.

Open Access Article. Published on 18 April 2016. Downloaded on 18/10/2016 21:34:14.
This article is licensed under a Creative Commons Attribution 3.0 Unported Licence.

33 W.-J. Kim, S. Kim, B. S. Lee, A. Kim, C. S. Ah, C. Huh, G. Y. Sung and W. S. Yun, *Langmuir*, 2009, **25**, 11692–11697.

34 Y. Wang, J. Miao, Y. Tian, C. Guo, J. Zhang, T. Ren and Q. Liu, *Opt. Express*, 2011, **19**, 17390–17395.

35 R. Kaliasas, J. Baltrusaitis, M. Mikolajūnas, L. Jakučionis and D. Viržonis, *Thin Solid Films*, 2012, **520**, 2041–2045.

36 A. P. Milenin, C. Jamois, T. Geppert, U. Gösele and R. B. Wehrspohn, *Microelectron. Eng.*, 2005, **81**, 15–21.

37 K. Suzuki, S.-W. Youn, Q. Wang, H. Hiroshima and Y. Nishioka, *Microelectron. Eng.*, 2013, **110**, 432–435.

38 A. Somashekhar, H. Ying, P. B. Smith, D. B. Aldrich and R. J. Nemanich, *J. Electrochem. Soc.*, 1999, **146**, 2318–2321.

39 K. Mohamed and M. M. Alkaisi, *Nanotechnology*, 2013, **24**, 015302.

40 K. P. Giapis, G. R. Scheller, R. A. Gottscho, W. S. Hobson and Y. H. Lee, *Appl. Phys. Lett.*, 1990, **57**, 983–985.

41 U. Diebold, *Surf. Sci. Rep.*, 2003, **48**, 53–229.

42 S. D. Chandradoss, A. C. Haagsma, Y. K. Lee, J.-H. Hwang, J.-M. Nam and C. Joo, *J. Visualized Exp.*, 2014, **86**, e50549.

43 H. Li, X. Zhang, X. Zhang, K. Wang, H. Liu and Y. Wei, *ACS Appl. Mater. Interfaces*, 2015, **7**, 4241–4246.

44 L. Chen, B. Yang and J. Zhang, *J. Adhes. Sci. Technol.*, 2014, **28**, 1725–1738.

45 Y. Nam, D. W. Branch and B. C. Wheeler, *Biosens. Bioelectron.*, 2006, **22**, 589–597.

46 Z. Ji, X. Jin, S. George, T. Xia, H. Meng, X. Wang, E. Suarez, H. Zhang, E. M. V. Hoek, H. Godwin, A. E. Nel and J. I. Zink, *Environ. Sci. Technol.*, 2010, **44**, 7309–7314.

47 B. Sweryda-Krawiec, H. Devaraj, G. Jacob and J. J. Hickman, *Langmuir*, 2004, **20**, 2054–2056.

48 C. Bouchiat, M. D. Wang, J.-F. Allemand, T. Strick, S. M. Block and V. Croquette, *Biophys. J.*, 1999, **76**, 409–413.

49 D. A. Koster, V. Croquette, C. Dekker, S. Shuman and N. H. Dekker, *Nature*, 2005, **434**, 671–674.

50 B. Gutiérrez-Medina, J. O. L. Andreasson, W. J. Greenleaf, A. Laporta and S. M. Block, *Methods Enzymol.*, 2010, **475**, 377–404.

51 P.-C. Li, J.-C. Chang, A. La Porta and E. T. Yu, *Nanotechnology*, 2014, **25**, 235304.

52 T. R. Strick, J.-F. Allemand, D. Bensimon, A. Bensimon and V. Croquette, *Science*, 1996, **271**, 1835–1837.

 This journal is © The Royal Society of Chemistry 2016

Electronic Supplementary Material (ESI) for Nanoscale.
This journal is © The Royal Society of Chemistry 2016

Supplementary Information

Tunable Top-Down Fabrication and Functional Surface Coating of Single-Crystal Titanium Dioxide Nanostructures and Nanoparticles

*Seungkyu Ha, Richard Janissen, Yera Ye. Ussembayev, Maarten M. van Oene, Belen Solano and Nynke H. Dekker**

Department of Bionanoscience, Kavli Institute of Nanoscience, Faculty of Applied Sciences, Delft University of Technology, Lorentzweg 1, 2628 CJ Delft, The Netherlands.

*E-mail: n.h.dekker@tudelft.nl

This document includes:

Supplementary Methods

Orientation of the optic axis in single-crystal rutile TiO_2 nanocylinder for OTW experiment.
Considerations for optimal fabrication of the Cr etch mask for single-crystal TiO_2 etching.
Surface functionalization procedure of single-crystal TiO_2.
Evaluation of single-crystal TiO_2 surface functionalization efficiency via fluorescence microscopy.
Preparation of DNA construct for OTW experiments.
Preparation of flow cell for OTW experiments.
Bioconjugation of DNA to single-crystal TiO_2 nanocylinders for OTW experiments.
OTW instrumentation and DNA measurements with single-crystal TiO_2 nanocylinders.

Supplementary Tables

Table S1. Dry etching conditions for single-crystal TiO_2 during optimization of the CHF_3-RIE process.
Table S2. Dry etching conditions for single-crystal TiO_2 nanofabrication.
Table S3. Dimensional analysis of high and low aspect-ratio TiO_2 nanocylinders.

Supplementary Figures

Fig. S1. Diverse applications of TiO_2 at the nanoscale.
Fig. S2. The etch rates and etch selectivities of different mask materials.
Fig. S3. Control of sidewall profiles and etch characteristics in single-crystal TiO_2 nanocylinders by variation of O_2 flow rate in the CHF_3-RIE process.
Fig. S4. Dimensions of fabricated single-crystal TiO_2 nanocylinders.
Fig. S5. Quantitative comparison of surface functionalization efficiencies on single-crystal TiO_2 for different linker molecules.
Fig. S6. DLS measurements of single-crystal TiO_2 nanocylinder aggregation in relation to surface coatings and buffer conditions.
Fig. S7. Optical trap calibration of single-crystal TiO_2 nanocylinders.

Supplementary References

Supplementary Methods

Orientation of the optic axis in single-crystal rutile TiO_2 nanocylinder for OTW experiment

To control polarization-based rotation of optically trapped nanoparticles in an OTW, birefringent positive uniaxial single-crystals are desirable substrate materials. Single-crystal rutile TiO_2 is such a material, and it has an exceptionally high birefringence that is advantageous for effective torque transfer in an OTW. In particular, cylindrically shaped nanoparticles align their long axis with the direction of laser beam propagation, fixing two of the three rotational degrees of freedom (DOF). The remaining rotational DOF is controllable via the polarization of the laser beam provided that the optic axis is perpendicular to the nanocylinder's long axis (**Fig. 5a**). To appropriately control the orientation of this optic axis within the nanocylinders, it is necessary to etch into (100)-cut single-crystal rutile TiO_2 substrates. A similar approach has been employed for the case of X-cut single-crystal quartz SiO_2 substrates.[1–5]

Considerations for optimal fabrication of the Cr etch mask for single-crystal TiO_2 etching

We consider the optimal fabrication of the Cr etch mask for the desired size of single-crystal TiO_2 nanostructures. The deposited Cr layer should be sufficiently thick for the mask to remain functional until the end of etching process, taking into account the fact that the mask top surface will not be perfectly flat. Also, the overall thickness of the Cr mask is limited by that of the used PMMA layer. The thickness of the PMMA should be 2−3 times larger than that of the Cr mask to facilitate complete lift-off, but it has an upper limit determined by its concentration. In practice, Cr layers thicker than ~150 nm tend to cause more severe deformation in patterned PMMA layers, resulting in higher nonuniformity. This deformation is presumably due to the built-up stress in Cr layers during physical vapor deposition.[6] A further consideration in mask fabrication is that mask shapes tend to be more cone-like when thicker Cr layers and/or smaller patterned apertures are used[7] (**Fig. 1**, **step 4**, **inset illustration**). Such masks are not suitable for anisotropic etching for vertical sidewall due to more rapid erosion of their thinner edges.

Surface functionalization procedure of single-crystal TiO_2

For the surface functionalization of single-crystal TiO_2 substrates, we have compared four different surface linker molecules (**Fig. S5**†): ETA (Sigma-Aldrich, The Netherlands), GPDMES (Sigma-Aldrich, The Netherlands), APDMES (Sigma-Aldrich, The Netherlands), and BADMSCP (abcr GmbH, Germany). For the binding of ETA linker, we dissolve ETA in anhydrous dimethyl sulfoxide (DMSO) (Sigma-Aldrich, The Netherlands) to a final concentration of 5 M. We use this ETA/DMSO solution to incubate the substrates for 12 h at room temperature, followed by washing the substrates with DI water. For the binding of epoxysilane linker (GPDMES), we incubate the substrates for 15 min at 75 °C using non-diluted GPDMES solution, followed by chloroform washing. For the binding of the APDMES and BADMSCP linkers, we incubate the substrates in ethanol containing either 5% (v/v) of APDMES or BADMSCP. We carry out the silanization reaction for 12 h at 70 °C and then wash with chloroform (or ethanol). Additionally, we perform PEGylation of ETA-coated surfaces with heterobifunctional NHS-PEG-COOH (MW 5,000, LaysanBio, USA).[8] We incubate the surfaces with 2 mM PEG dissolved in 100 mM 2-(N-morpholino)ethanesulfonic acid (MES) buffer (pH 4.7, Sigma-Aldrich, The Netherlands) for 1 h at room

temperature. Afterwards, we wash the PEGylated surfaces with DI water. For every washing step involved, we wash three times for 15 s each, and then dry the substrates under a N_2 stream. The above protocols can also be applied to other oxidized surfaces, e.g. quartz (SiO_2) (**Fig. S5**†), silicon (Si), silicon nitride (Si_3N_4), and non-noble metals.

Evaluation of single-crystal TiO_2 surface functionalization efficiency via fluorescence microscopy

We fabricate 25 × 25 μm^2 micro-patterns of PMMA on single-crystal rutile TiO_2 and quartz SiO_2 substrates for quantitative evaluation of the surface linker functionalization efficiencies via fluorescence microscopy. To fabricate the PMMA micro-patterns, we utilize a similar protocol as described for TiO_2 nanocylinders (**Methods**). The main differences include spin-coating PMMA 950k A11 to achieve a ~1.9 µm-thick layer and altered e-beam settings (a current of 312 nA, a diameter of 300 nm through defocusing the beam, and a dose of 1000 $\mu C/cm^2$). For the quartz SiO_2 substrates (X-cut, University Wafer, USA) alone, we sputter a 30 nm-thick gold (Au) layer (EM ACE600, Leica, The Netherlands) onto the spin-coated PMMA layer to prevent charging. Following e-beam patterning, we remove the Au layer by a wet etchant (TFA, Transene, USA). As described in **Methods**, we treat the micro-patterned substrates with O_2 plasma (Plasma-PREEN I) prior to the functionalization process.

For the evaluation of the surface functionalization efficiencies of the different linkers to single-crystal TiO_2 (and SiO_2) substrates, we use amino and NHS-ester modified fluorophores (ATTO 647N, ATTO-TEC GmbH, Germany). They are covalently added to the organic functional groups of the surface linkers employed. For the substrates coated with ETA, APDMES, and BADMSCP, we dissolve NHS-ester labeled fluorophores in PBS buffer (pH 8.4, Sigma-Aldrich, The Netherlands) to a final concentration of 10 µM and add to the functionalized surfaces. After the reaction time of 1 h, we wash the substrates three times each with PBS/TWEEN® buffer (pH 7.4) and DI water to remove residual physisorbed molecules, and dry under a N_2 stream. For GPDMES-coated and PEGylated surfaces, we add 10 µM of amino-labeled fluorophores to PBS buffer (pH 7.4) and MES/EDC buffer (100 mM MES (pH 4.7) containing 50 mM EDC (1-Ethyl-3-(3-dimethylaminopropyl)carbodiimid, Sigma-Aldrich, The Netherlands)), respectively, and the fluorophore coupling reactions take place for 1 h. We wash the substrates with PBS/TWEEN® buffer (pH 7.4) and DI water, followed by drying under a N_2 stream, as stated before.

We perform the fluorescence measurements of the functionalized surfaces and nanocylinders using an epifluorescence microscope (IX-81, Olympus, The Netherlands) equipped with a Peltier-cooled back-illuminated electron multiplying charge coupled device (EMCCD) camera (IXON, 512 × 512 pixels, Andor, Ireland), in combination with an oil-immersion objective lens (100×/NA1.3, UPLNFLN, Olympus, The Netherlands). The fluorophores are excited using a diode laser (λ = 640 nm, Cell Laser System, Olympus, The Netherlands). For quantitative measurements, we measure the fluorescence intensity (in photon counts per second) of an area of 12.5 × 12.5 μm^2 for different square micro-patterns on each sample. We calculate the average intensity – normalized to the area of 1 μm^2 – and the corresponding standard deviations to compare the different linker molecule coverages (**Fig. S5**†).

Preparation of DNA construct for OTW experiments

We carry out the DNA extension and supercoiling measurements (**Fig. 5**) on a linear 21.8 kbp DNA that contains biotin and digoxigenin modified nucleotides (biotin-16-dUTP and digoxigenin-11-dUTP, respectively, Roche Diagnostics, The Netherlands) at the opposite extremities (600 bp each). We prepare the DNA by ligating the biotin- and digoxigenin-enriched handles to a 20.6 kbp DNA fragment that is obtained via a *Not*I/*Xho*I digestion of Supercos1-lambda 1,2 plasmid (Agilent Technologies, USA). We create the DNA handles by PCR amplification of a 1.2 kbp fragment from pBlueScript II SK+ (Agilent Technologies, USA) using the primers − 5'-GACCGAGATAGGGTTGAGTG and 5'-CAGGGTCGGAACAGGAGAGC − in the presence of either biotin-16-dUTP or digoxigenin-11-dUTP. Prior to ligation using T4 DNA ligase (New England Biolabs, UK), the biotin and digoxigenin containing handles are digested with *Not*I and *Xho*I, respectively.[9]

Preparation of flow cell for OTW experiments

We perform OTW experiments (**Fig. 5**) in a custom-made flow cell assembled from two 24 × 60 mm^2 borosilicate coverslips (#1.5, ~170 µm thickness, Menzel GmbH, Germany) separated by a single-layer Parafilm® (Sigma-Aldrich, The Netherlands) spacer.[1,8,10] We drill two holes of ~1 mm diameter in the top coverslips using a sand blaster, to connect with inlet and outlet tubings. Prior to flow cell assembly, we clean the coverslips using a 4% (v/v) aqueous Hellmanex® III (Hellma GmbH, Germany) solution and then DI water, in both cases by sonication for 20 min at 40 °C. We dry the cleaned coverslips under a N_2 stream. For the bottom coverslips, we perform surface functionalization to attach biomolecules. To increase the density of surface hydroxyl groups, which allows for denser, more homogeneous functionalization, we treat the bottom coverslips with O_2 plasma (Plasma-PREEN I) for 1 min with O_2 flow rate of 3 scfh and RF power of 200 W. We incubate these coverslips in DMSO solution containing 5 M ETA for 12 h at room temperature. Afterwards, we wash the functionalized coverslips thoroughly with DI water and dry them under a N_2 stream. Single-layer Parafilm® spacers are prepared by cutting out the desired flow cell channel shape, which is properly aligned to the holes in the top coverslips. Finally, we assemble the flow cells and seal the channels by melting the Parafilm® spacers between the coverslips on a hotplate for 30 s at 90 °C.

Bioconjugation of DNA to single-crystal TiO_2 nanocylinders for OTW experiments

In an OTW, we are able to carry out the extension and coiling measurements on individual, torsionally constrained DNA molecules.[1–5] We tether the DNA molecules to the bottom surface of the flow cell channel via digoxigenin:anti-digoxigenin coupling and to the functionalized single-crystal rutile TiO_2 nanocylinders via biotin:streptavidin coupling (**Fig. 5a**). To do so, we perform three steps. First, we PEGylate the ETA-coated flow cell channel both to covalently attach digoxigenin antibodies and to ensure an effective surface passivation against non-specific physisorption of streptavidin-coated TiO_2 nanocylinders. We achieve this by incubating the channel with 2 mM PEG dissolved in 100 mM MES buffer (pH 4.7) for 1 h. After washing with DI water, we incubate for 1 h with 8 µM digoxigenin IgG antibodies (Roche Diagnostics, The Netherlands) dissolved in MES/EDC buffer (pH 4.7). We wash the channel with PBS buffer (pH 7.4) and incubate BlockAid™ (Life

Technologies, USA) for 1 h for additional surface passivation. Subsequently, we wash the channel with PBS buffer (pH 7.4). Second, we attach individual DNA molecules via the digoxigenin handles to the digoxigenin antibody-covered flow cell channel by incubating 5 pM of DNA for 1 h. We remove non-specifically adhered DNA molecules by washing the channel with PBS buffer (pH 7.4). Third, we attach the DNA via the biotinylated handles to the streptavidin-coated TiO_2 nanocylinders (**Methods**) by incubating them in the flow cell channel for ~30 min. We remove non-attached nanocylinders by flushing 1:1 diluted (v/v) BlockAid™ in PBS/Triton™ buffer (pH 7.4). We perform all DNA extension and coiling measurements in PBS/Triton™ buffer.

OTW instrumentation and DNA measurements with single-crystal TiO_2 nanocylinders

For optical trapping of single-crystal TiO_2 nanocylinders in our OTW setup (**Fig. 5b,c**), we expand and collimate a linearly polarized laser (λ = 1064 nm, Compass CW 1064-4000M, Coherent, The Netherlands) beam using a beam expander (4401-181-000-20, LINOS, Germany) to fill properly the input aperture of an objective lens (60×/NA1.2, CFI-PLAN-APO-VC-60XA-WI, Nikon, The Netherlands). The power entering the objective lens is always set to 100 mW during experiments. The objective lens focuses the laser beam into a flow cell, generating an optical trap.

To calibrate the optical trap, we monitor the fluctuations of an isolated, optically trapped TiO_2 nanocylinder using a position-sensitive detector (PSD) (DL100-7PCBA3, Pacific Silicon Sensor, The Netherlands) that acquires at 100 kHz (**Fig. S7**†). The nanocylinder trapping position is ~7 μm above from the bottom surface of the flow cell channel, to conserve the similar measurement conditions with the case of DNA-tethered nanocylinders.[11] We can calculate the restoring force acting on a nanocylinder displaced from the trap center, by multiplying the measured displacement with the calibrated trap stiffness. Precise linear translation of the flow cell is possible using a piezo-actuator (P-517.3CD, Physik Instrumente, Germany) in x, y, and z directions.

For the force-induced DNA-extension experiments, we move the flow cell along the axis of laser beam propagation (axial direction) at a constant speed (~1 μm/s) while maintaining the laser beam at a fixed position. As the flow cell moves away from the laser beam focus, the increased DNA-tethered nanocylinder's displacement from the trap center induces higher axial force to the DNA molecule. For the DNA coiling experiments, a constant axial force should be applied to the trapped, DNA-tethered nanocylinder since whether the DNA twists or forms plectonemic supercoils strongly influenced by the tension applied to the molecule.[12] We use a feedback loop between the piezo-actuator and PSD to clamp the axial force at the specified setpoint. By simultaneously rotating the linear input polarization of the laser beam, we apply torque to the TiO_2 nanocylinder, coiling the DNA molecule. The polarization can be rotated either by manual rotation of a half-wave plate (PWPS-1064-10-2, CVI Melles Griot, Germany), or by a fast electro-optical modulator (EOM) (LM 0202-LT, LINOS, Germany) in combination with quarter-wave plates (PWPS-1064-10-4, CVI Melles Griot, Germany).

Supplementary Tables

Table S1. Dry etching conditions for single-crystal TiO_2 during optimization of the CHF_3-RIE process.[a)]

Sample	CHF_3 flow [sccm]	O_2 flow [sccm]	Ar flow [sccm]	RF power [W]	Chamber pressure [µbar]	TiO_2 etch rate [nm/min]	Cr etch rate [nm/min]	Etch selectivity [TiO_2:Cr]
Ra1	50	5	30	200	50	68	3.7	18
Ra2	50	5	30	**165**	50	58	3.2	18
Ra3	50	5	30	**100**	50	30	1.7	18
Ra4	50	5	30	200	**10**	30	8.3	4
Rb1	50	5	30	200	50	77	4.1	19
Rb2	50	5	**0**	200	50	73	3.5	21

[a)] The bold red numbers denote altered process parameters compared to the reference samples (Ra1 and Rb1).

Dry etching conditions for single-crystal TiO_2 during optimization of the CHF_3-RIE process

We show the representative etching conditions (**Table S1**†) used during optimization of the CHF_3-based plasma etching of single-crystal TiO_2 in an RIE system. Throughout the optimization, we fix the flow rate of CHF_3 gas, the main etchant, at the maximum value of 50 sccm, and set the flow rate of O_2 gas at 5 sccm which is the median value of our target range (0–10 sccm). More accurate comparisons are possible within the same batches of the applied Cr etch mask, designated as Ra (H: 100 nm, D: 535 nm) and Rb (H: 100 nm, D: 345 nm). The samples Ra1 and Rb1 are the reference samples, while the other samples differ by a single process parameter (designated as bold red numbers in **Table S1**†).

As an elevated RF power increases the etch rates of TiO_2 while maintaining nearly constant etch selectivity (compare samples Ra1, Ra2, and Ra3 in **Table S1**†), we select the highest available power (200 W). We find that an increase in the chamber pressure (from 10 to 50 µbar) enhances the etch selectivity by increasing the TiO_2 etch rates and decreasing the Cr etch rates (compare samples Ra1 and Ra4 in **Table S1**†). However, we do not utilize chamber pressures exceeding 50 µbar, as higher values result in excessive deposition of fluorocarbon passivation layers[13] that are sufficiently thick to reduce the TiO_2 etch rates again. With these parameters fixed, we vary the gas composition. The addition of Ar gas, which results in harsher physical etching by heavy ions, generally increases etch rates.[14] Indeed, upon its addition (at 30 sccm) both the Cr and TiO_2 etch rates are increased; however, as the increase in the Cr etch rate surpasses that of TiO_2, a deteriorated etch selectivity results (compare samples Rb1 and Rb2 in **Table S1**†). Our optimized process condition thus consists of CHF_3 at 50 sccm, a chamber pressure of 50 µbar, and an RF power of 200 W. With these fixed parameters, we vary O_2 gas flow rate from 0 sccm to 10 sccm to control sidewall profiles (**Fig. S3**†), and vertical sidewall can be obtained with 0.5 sccm of O_2.

Table S2. Dry etching conditions for single-crystal TiO_2 nanofabrication.[a)]

Figure	Etching System	Etching conditions
Fig. 2a	F1	Cr etch mask (H: 45 nm, D: 175 nm), **CHF_3**:O_2 = 50:0.5 sccm, RF 200 W, chamber pressure 50 µbar, DC bias -950 V, etch time 11 min (**optimized**).
Fig. 2b	F2	Cr etch mask (H: 100 nm, D: 255 nm), **CHF_3**:O_2 = 50:8 sccm, RF 200 W, chamber pressure 50 µbar, DC bias -1100 V, etch time 15 min (**optimized**).
Fig. 2c	F1	Cr etch mask (H: 100 nm, D: 535 nm), **CHF_3**:O_2:Ar = 50:5:30 sccm, RF 165 W, chamber pressure 50 µbar, DC bias -855 V, etch time 15 min.
Fig. 2d	F3	Cr etch mask (H: 100 nm, D: 535 nm), **SF_6**:CH_4:Ar = 15:30:50 sccm, ICP:RF = 2500:300 W, chamber pressure 30 µbar, DC bias -50 V, etch time 10 min, sample holder temperature 0 °C, chamber temperature 200 °C.
Fig. 2e	F4	Cr etch mask (H: 130 nm, D: 185 nm), **SF_6**:He = 50:100 sccm, ICP:RF = 800:200 W, chamber pressure 50 µbar, DC bias -475 V, etch time 12 min, chamber temperature 25 °C.
Fig. 2f	F4	Cr etch mask (H: 120 nm, D: 205 nm), **SF_6**:He = 20:100 sccm, ICP:RF = 300:300 W, chamber pressure 100 µbar, DC bias -835 V, etch time 4 min, chamber temperature 25 °C (**optimized**).
Fig. 3	F2	Cr etch mask (H: 60 nm, D: 220 nm), **CHF_3**:O_2 = 50:4 sccm, RF 200 W, chamber pressure 50 µbar, DC bias -1100 V, etch time 15 min (**optimized**).
Fig. 5	F4	Cr etch mask, the same etching condition as **Fig. 2f (**SF_6**)**.
Fig. S2†	F3	Various etch mask materials, **SF_6**:CH_4:Ar = 15:30:50 sccm, ICP:RF = 1500:250 W, chamber pressure 30 µbar, DC bias -55 V, etch time 10 min, sample holder temperature 0 °C, chamber temperature 200 °C.
Fig. S3†	F1	Cr etch mask (H: 100 nm, D: 345 nm), the same etching condition as **Fig. 2a (**CHF_3**),** except for the etch time (15 min) and the O_2 gas flow rate (0, 0.5, 1, 5, or 10 sccm).
Fig. S4†	F2	Cr etch mask (H: 30 nm, D: 190 nm), the same etching condition as **Fig. 3 (**CHF_3**)**, except for the etch time (8 min).
Fig. S7†	F4	Cr etch mask, the same etching condition as **Fig. 2f (**SF_6**)**.

[a)] The bold red letters denote the main etchant gas in each condition.

Dry etching conditions for single-crystal TiO_2 nanofabrication

We use etching systems that are denoted as F1 (Fluor Z401S, Leybold Heraeus, Germany), F2 (Fluor Z401S, Leybold Heraeus, Germany), F3 (AMS100 I-speeder, Adixen, France), and F4 (Plasmalab System 100, Oxford Instr., UK). The F1 and F2 are two nominally identical RIE systems, while F3 and F4 are two distinct ICP-RIE systems. We summarize the etching conditions for each batch of TiO_2 nanocylinders in **Table S2**†.

Table S3. Dimensional analysis of high and low aspect-ratio TiO_2 nanocylinders.

Sample	Statistical parameter	Top diameter	Bottom diameter	Height	Top roundness	Bottom roundness	Volume
Fig. 3 (15 min etch)	Average	151 nm	215 nm	652 nm	0.97	0.98	0.017 μm^3
	Local RSD	4.4%	2.3%	0.6%	1.0%	0.5%	4.5%
	Global RSD	4.7%	2.7%	1.4%	1.1%	0.5%	5.2%
Fig. S4† (8 min etch)	Average	149 nm	187 nm	273 nm	0.98	0.99	0.006 μm^3
	Local RSD	1.5%	0.9%	1.3%	0.5%	0.3%	2.1%
	Global RSD	2.4%	1.7%	3.1%	0.6%	0.4%	4.1%

Dimensional analysis of high and low aspect-ratio TiO_2 nanocylinders

We have analyzed SEM images of high and low aspect-ratio nanocylinder batches to quantify both the local and global structural uniformity. We summarize the obtained statistical parameters for each batch of TiO_2 nanocylinders in **Table S3†**, and present the corresponding graphs in **Fig. 3d-f** (high aspect-ratio: 3.6) and **Fig. S4d-i†** (low aspect-ratio: 1.6).

Supplementary Figures

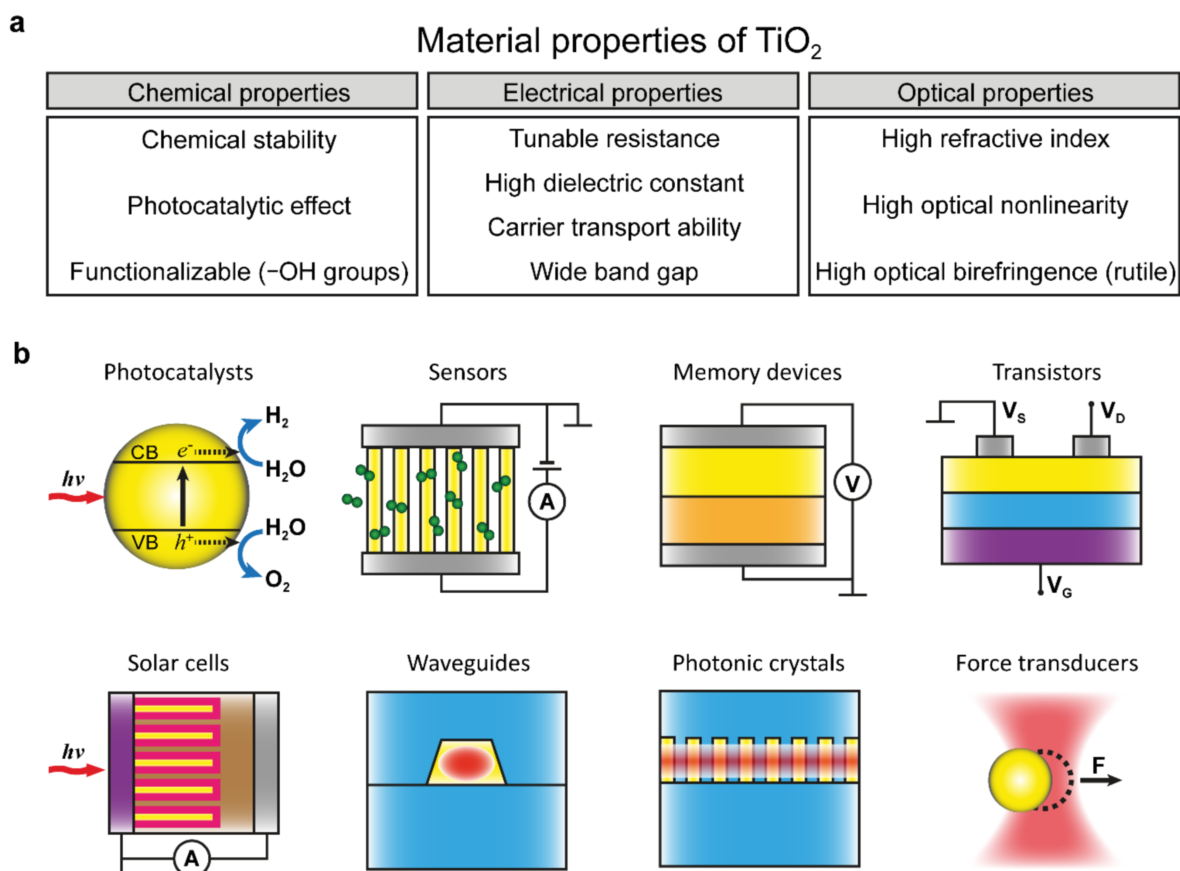

Fig. S1. Diverse applications of TiO_2 at the nanoscale. **(a)** Overview of the chemical, electrical, and optical properties that make TiO_2 a versatile material for different applications. **(b)** Illustrations of nanoscale applications of TiO_2 (yellow). Top, left to right: a TiO_2 nanoparticle serves as a photocatalyst for water splitting into oxygen and hydrogen gases ($h\nu$: input radiation energy, CB: conduction band, VB: valence band, e^-: electron, h^+: hole); a TiO_2 nanopillar array acts as a gas sensor (gray: metal electrodes, green: gas molecules, A: current as a sensing signal); a TiO_2 thin film acts as a tunable resistance material in a resistive random access memory device (gray: metal electrodes, orange: TiO_{2-x}, V: voltage as a read/write signal); a TiO_2 thin film can be used as a channel layer in a transparent transistor (gray: metal electrodes, blue: gate insulator, purple: transparent electrode, V_S, V_D, and V_G denote voltages at source, drain, and gate terminals, respectively). Bottom, left to right: a TiO_2 nanorod array acts as a photoanode in a solar cell ($h\nu$: radiation energy from the sun, gray: metal electrode, purple: transparent electrode, magenta: sensitization layer e.g. dye molecules or quantum dots, brown: electrolyte, A: current as converted energy); a nanostructured TiO_2 forms the core of a strip waveguide to support lightwave propagation (blue: cladding layers, red: confined lightwave); a two-dimensional TiO_2 photonic crystal slab used to manipulate the flow of lightwave (blue: cladding layers, red: confined lightwave); an optically trapped TiO_2 nanoparticle used as a force transducer (red: focused laser beam, dotted circle: trap center, F: force induced by the displacement of the nanoparticle).

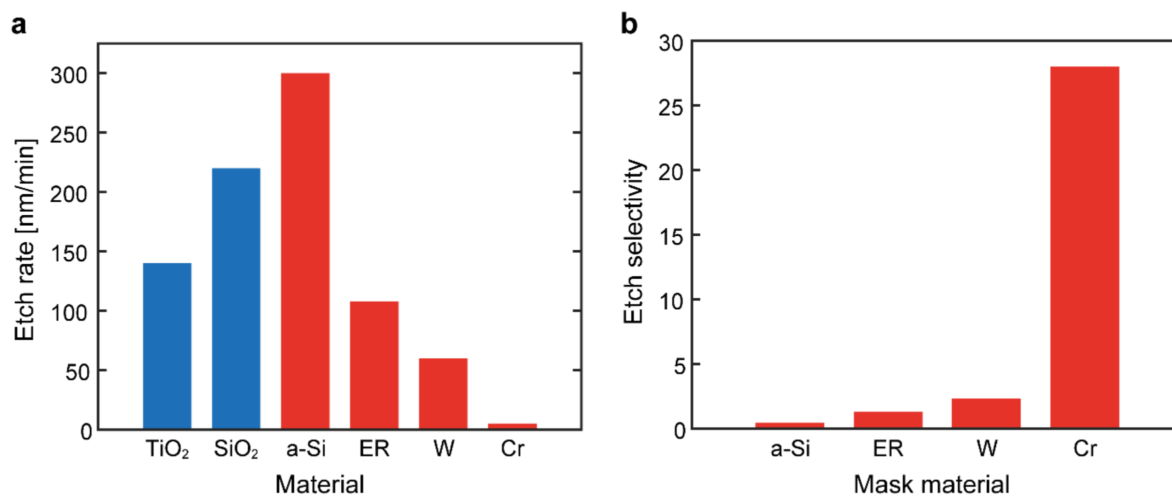

Fig. S2. The etch rates and etch selectivities of different mask materials. **(a)** The etch rates for substrate (blue bars) materials (TiO_2: (100)-cut rutile single crystal, ~140 nm/min; SiO_2: X-cut quartz single crystal, ~220 nm/min) and mask (red bars) materials (a-Si: amorphous silicon layer deposited by a plasma-enhanced chemical vapor deposition system (Plasmalab 80 Plus, Oxford Instr., UK), ~300 nm/min; ER: spin-coated and baked e-beam resist layer (NEB-22A2E, Sumitomo Chemical, Belgium), ~110 nm/min; W: tungsten layer deposited by an e-beam evaporator (Temescal FC-2000, Ferrotec, Germany), ~60 nm/min; Cr: chromium layer deposited by the same evaporator, ~5 nm/min). All results are obtained under the same dry etching conditions (using the F3 etching system; etching conditions in **Table S2**†). **(b)** Etch selectivity of each mask material for single-crystal TiO_2 dry etching, which is the etch rate of TiO_2 divided by that of the mask material (a-Si: 0.5, ER: 1.3, W: 2.3, Cr: 28).

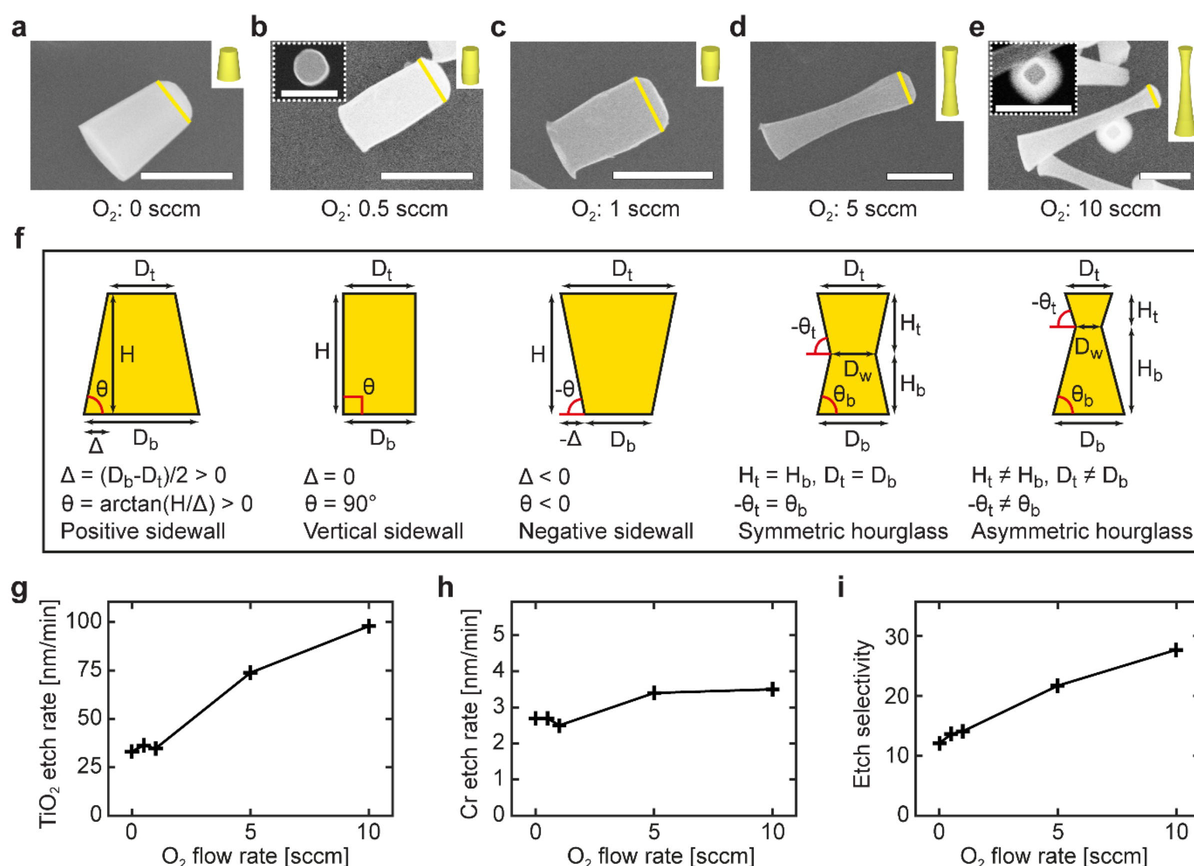

Fig. S3. Control of sidewall profiles and etch characteristics in single-crystal TiO_2 nanocylinders by variation of O_2 flow rate in the CHF_3-RIE process. **(a-e)** SEM images of single-crystal TiO_2 nanocylinders produced under identical etching conditions (using the F1 etching system; etching conditions in **Table S2**†) apart from the O_2 flow rate (values shown at the bottom of each image). Scale bars denote 500 nm. Top surfaces of the nanocylinders are marked with yellow lines because the remaining Cr masks are also visible in these images. The insets in top-right corner illustrate (to scale) the corresponding three-dimensional shapes of the nanocylinder SEM images. The types of obtained nanocylinder shapes include **(a)** positive sidewall angles, **(b)** vertical sidewall angles, **(c)** negative sidewall angles, **(d)** symmetric hourglass shapes, and **(e)** asymmetric hourglass shapes. In **(b)** and **(e)**, the insets in top-left corner (scale bars denote 500 nm) show top-view SEM images of nanocylinders cut at their middle, displaying cross-sections that are **(b)** circular or **(e)** diamond-shaped. **(f)** For the analysis of sidewall angles (θ), we use two-dimensional models as defined here. The definition of sidewall angles is illustrated for the cases of positive, vertical, and negative angles, using the measured heights (H) and diameters of top (D_t) and bottom (D_b). The hourglass-shaped nanocylinders possess two sidewall angles and heights for both top (θ_t, H_t) and bottom (θ_b, H_b) sides, and an additional waist diameter (D_w). **(g-i)** The etch characteristics are shown as a function of the O_2 flow rate: the etch rates of **(g)** TiO_2, **(h)** Cr, and **(i)** the resulting etch selectivities (TiO_2:Cr). The measured dimensions extracted from the SEM images **(a-e)** are as follows: **(a)** D_t: 285 nm, D_b: 395 nm, H: 500 nm, θ: 84°; **(b)** $D_t = D_b$: 275 nm, H: 545, θ: 90°; **(c)** D_t: 305 nm, D_b: 260 nm, H: 520 nm, θ: -88°; **(d)** $D_t = D_b$: 260 nm, D_w: 175 nm, $H_t = H_b$: 555 nm, $-\theta_t = \theta_b$: 86°; **(e)** D_t: 245 nm, D_b: 370 nm, D_w: 135 nm, H_t: 385 nm, H_b: 1085 nm, θ_t: -82°, θ_b: 84°.

Control mechanism for sidewall profiles in CHF_3-etched single-crystal TiO_2 nanocylinders

We observe that tuning the O_2 flow rate during the single-crystal TiO_2 etching process allows us to control the sidewall profile of the nanostructures. We attribute the formation of different sidewall profiles (positive, vertical, negative, and hourglass-shaped) to underlying changes in the thickness of a sidewall passivation layer that result from the interplay between CHF_3 and O_2 plasma. The thickness variation permits both the formation

of positive sidewall angles in the absence of O_2 flow and the formation of vertical (or negative) sidewall angles at an O_2 flow of 0.5 (1.0) sccm (**Fig. S3a-c†**). The hourglass-shaped etch profiles likely result from substantially reduced TiO_2 surface passivation combined with the random trajectories of reactive ions[15,16] (**Fig. S3d,e†**).

Control mechanism for cross-sectional shapes and etch selectivity in CHF_3-etched single-crystal TiO_2 nanocylinders

We find that the single-crystal TiO_2 nanocylinders etched at low O_2 flow rates (0−1 sccm) exhibit circular cross-sections (**Fig. S3b†, inset** in top-left corner), while those etched at high O_2 flow rates (5−10 sccm) feature diamond-shaped cross-sections (**Fig. S3e†, inset** in top-left corner). These differences may result from changes in the predominant etching mode: at low O_2 flow rates, the initial shape of the etch masks (circular in the case of **Fig. S3†**) should be directly transferred to the etched nanostructures, as the dominance of physical etching by ion bombardment results in the same etch rate independently of crystallographic orientation; conversely, at high O_2 flow rates, chemical etching may predominate than physical etching, resulting in etch rates that vary per orientation of the crystal planes in the single-crystal TiO_2 substrates.[17] Moreover, the above reasoning is supported by the fact that TiO_2 etch rates (**Fig. S3g†**) increase significantly (~3-fold) while Cr etch rates (**Fig. S3h†**) remain nearly the constant (~3 nm/min), as we increase O_2 flow rate. The removal of Cr mask layer is possible only by the physical etching but not by the chemical etching based on fluorine chemistry while both etching modes induce TiO_2 etching. We attribute this to a decreased thickness of the CHF_3 plasma-generated fluorocarbon passivation layer on TiO_2 surfaces in the presence of O_2 plasma.[18] As such a layer protects TiO_2 surfaces from chemical reaction with etching species, its decreased thickness results in an increase of the TiO_2 etch rates whilst those of Cr remain nearly unaffected, enhancing etch selectivity (**Fig. S3i†**).

The reproducibility of different sidewall profiles in CHF_3-etched single-crystal TiO_2 nanocylinders

A repetition of this experiment in the second nominally identical RIE system yields the similar trends but at slightly altered O_2 flow rates (using the F2 etching system; etching conditions in **Table S2†**). For example, etching nanocylinders with vertical sidewall angles requires an O_2 flow rate of 4−8 sccm (compared to ~0.5 sccm in the first RIE system (**Fig. S3b†**)). Similarly, etching nanocylinders into hourglass-shapes requires an O_2 flow rate of ~16 sccm (compared to 5−10 sccm in the first RIE system (**Fig. S3d,e†**)). We attribute this discrepancies in parameters to the differences in instrument calibration, e.g. of the mass flow controllers for the control and measurement of O_2 flow rates.

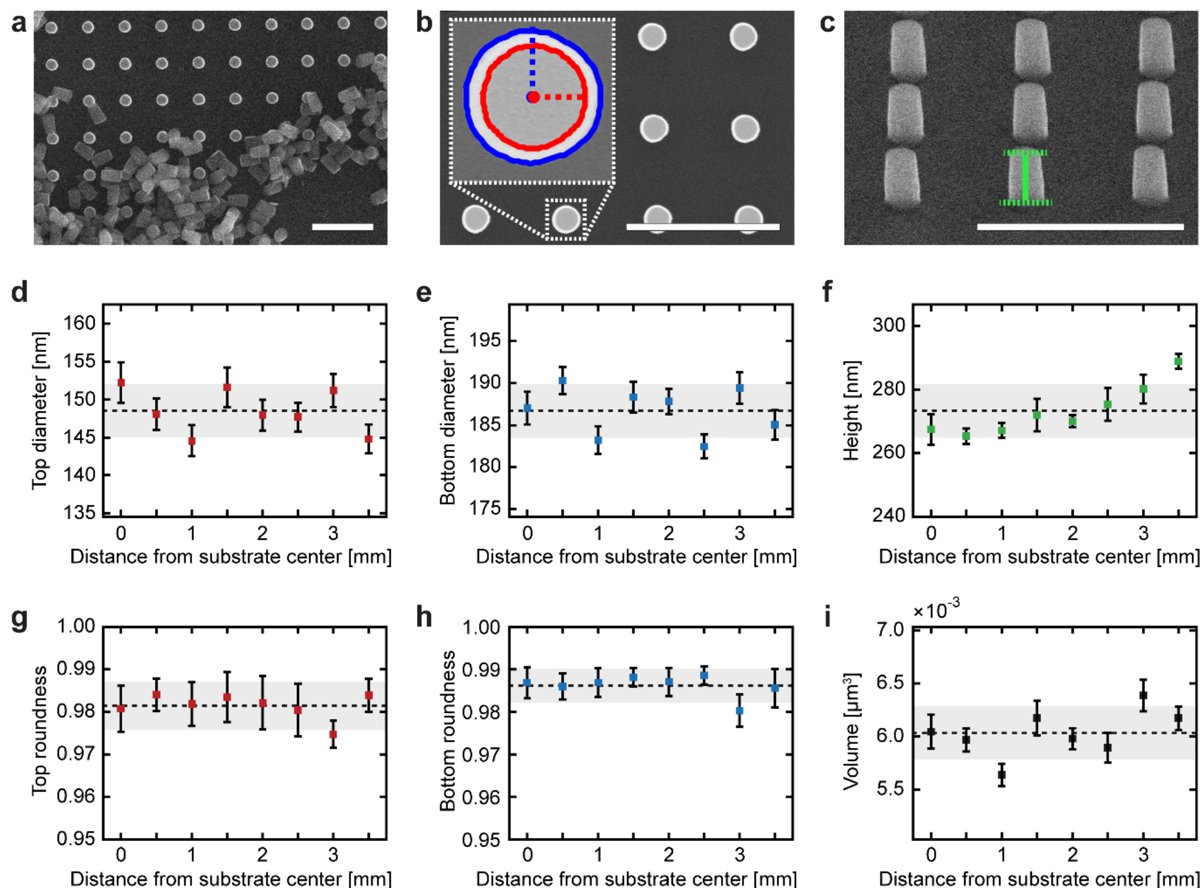

Fig. S4. Dimensions of fabricated single-crystal TiO_2 nanocylinders. **(a-c)** SEM images of etched single-crystal TiO_2 nanocylinders (light gray). Scale bars denote 1 µm. **(a)** Top-view of a single-crystal TiO_2 substrate with partially cleaved nanocylinders. An array of rigidly fixed nanocylinders is visible in the top left corner, and the cleaved substrate surface is bottom right corner. The released nanocylinders are positioned at the interface of these regions. **(b)** Top-view of a substrate with etched nanocylinders. The inset shows a zoom-in as an example for image analysis. The red (blue) contour, dotted line, and dot represent the boundary, equivalent radius, and center of nanocylinder top (bottom) surface, respectively. **(c)** Tilted-view (60°) of a substrate with etched nanocylinders. The green dotted horizontal lines are crossing the centers of top and bottom surfaces, and the green vertical line indicates the height that will be converted to the actual height considering the tilting angle. **(d-i)** Nanocylinder dimensions extracted from the SEM images. The graphs display the **(d)** top diameter, **(e)** bottom diameter, **(f)** height, **(g)** top roundness, **(h)** bottom roundness, and **(i)** volume as a function of the radial distance from the substrate center. The roundness (defined as $4\pi A/P^2$, A: area, P: perimeter) measures how closely the shape of a nanocylinder's cross section resembles that of a circle, where 1 corresponds to a perfect circle and smaller values imply deviations from circular. Measurement points are spaced by 0.5 mm from the center of the substrate to its edge. At each point, the diameters (heights) are calculated from $n = 12$ ($n = 10$) different nanocylinders. The square markers and the error bars in the graphs represent the mean and the standard deviation of the local uniformity, respectively. The horizontal dotted black lines and the top and bottom sides of the gray shaded boxes in the graphs represent the mean and the standard deviation of the global uniformity, respectively.

Distributions of fabricated single-crystal TiO_2 nanocylinder dimensions

The comparison between single-crystal TiO_2 nanocylinder dimensions presented in **Fig. S4**† and those presented earlier (**Fig. 3**) provides more information for the analysis of the nanocylinder dimensions. We etch the different batches of nanocylinders under the same conditions, except for the etch duration (**Table S2**†). The etch time of the nanocylinders analyzed in **Fig. S4**† (8 min) is approximately twice less than that of the

nanocylinders shown in **Fig. 3** (15 min). Both etch times demonstrate a similar trend regarding the nanocylinder dimensions (analysis results are summarized in **Table S3**†). The observed irregular Cr mask erosion effect, which depends on the roughness of the mask surface, causes stronger deformation of the top surface geometry than the bottom of the nanocylinders; we expect that the bottom surface geometry is mostly determined by the initial round shape of etch mask while the top surface geometry is the same as the eroded etch mask until the end of the etching process. This geometry deformation is also observable in the roundness analysis, in which the top roundness values are smaller than the bottom roundness values for both batches of nanocylinders. For this reason, the top diameters show less local uniformity than the bottom diameters. As this effect is more profound for extended etch times, etch time of 15 min results in less local uniformity than etch time of 8 min for both top and bottom diameters. For each measurement point, the top and bottom diameters are directly correlated as observable in **Fig. S4**† and **Fig. 3**. However, variations in the top and bottom diameters across a substrate are random, possibly due to the instability of e-beam size or current during e-beam patterning process. Regardless of these variations, the top and bottom diameters exhibit still high global uniformity for both batches of nanocylinders (RSD ≤5%), which lie in the same order of magnitude as their local uniformity. Further, we observe high global uniformity in nanocylinder heights across the substrates (RSD ≤3%) regardless of the loading effect. These excellent global uniformity in both diameters and heights leads to nanocylinder volumes with high global uniformity (RSD ≤5%) across a substrate which is desirable for the application of torque in an OTW.[1]

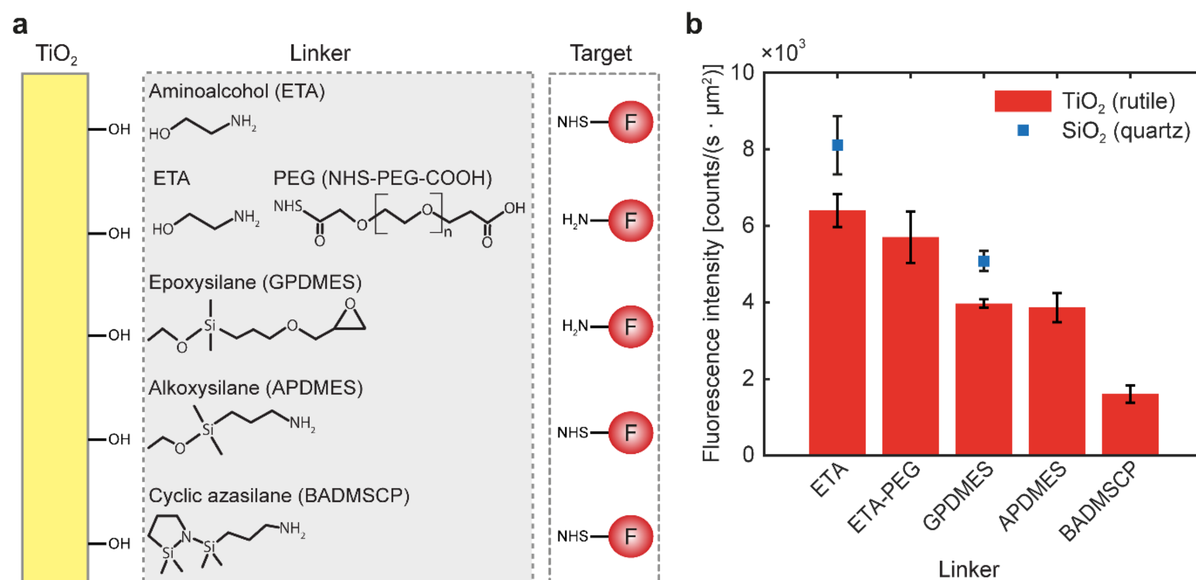

Fig. S5. Quantitative comparison of surface functionalization efficiencies on single-crystal TiO_2 for different linker molecules. **(a)** Schematic of the different functionalization strategies. At left, the TiO_2 (or other oxide materials, e.g. SiO_2) surface provides hydroxyl groups (-OH) to which the linkers bind covalently. In the center, the used linker molecules (ETA, GPDMES, APDMES, and BADMSCP) are shown with their molecular structures, including the PEGylation of ETA-coated surface. At right, target molecules are NHS-ester or amine modified ATTO 647N fluorophores (F), binding to the different functional group of each linker (**ESI Methods**†). The fluorophores allow quantitative measurements via fluorescence microscopy. However, in the same manner, other organic molecules, such as biomolecules or polymers, can be bound to the surface linkers. **(b)** Quantitative comparison of differently functionalized single-crystal rutile TiO_2 (red bars) and quartz SiO_2 (blue squares) substrates. The measured fluorescence intensity represents the surface coating density while the error bar (standard deviation) reflects the homogeneity of the coatings (**ESI Methods**†).

Comparison of TiO_2 and SiO_2 in surface functionalization efficiency

It is known that TiO_2 has lower functionalization efficiency compared to other widely used oxide materials, e.g. SiO_2 and Al_2O_3.[19,20] To quantify this difference in functionalization efficiency, we compare the surface coating efficiency of TiO_2 (rutile) with that of SiO_2 (quartz). We select two linkers for this comparison: ETA, based on its highest coating efficiency on TiO_2 surfaces (**Fig. S5b**†), and GPDMES that we used for TiO_2 nanostructure functionalization (**Fig. 4c**) and OTW measurements (**Fig. 5**). For SiO_2 substrates, which are functionalized under the same conditions as TiO_2, both ETA and GPDMES coatings show ~30% higher functionalization density than on TiO_2. However, the coating efficiencies of TiO_2 are sufficient to perform single molecule OTW experiments (**Fig. 5b,c**). If higher coating density is required, TiO_2 substrates can be treated with extended O_2 plasma-treatment time to increase the density of surface hydroxyl groups.[20]

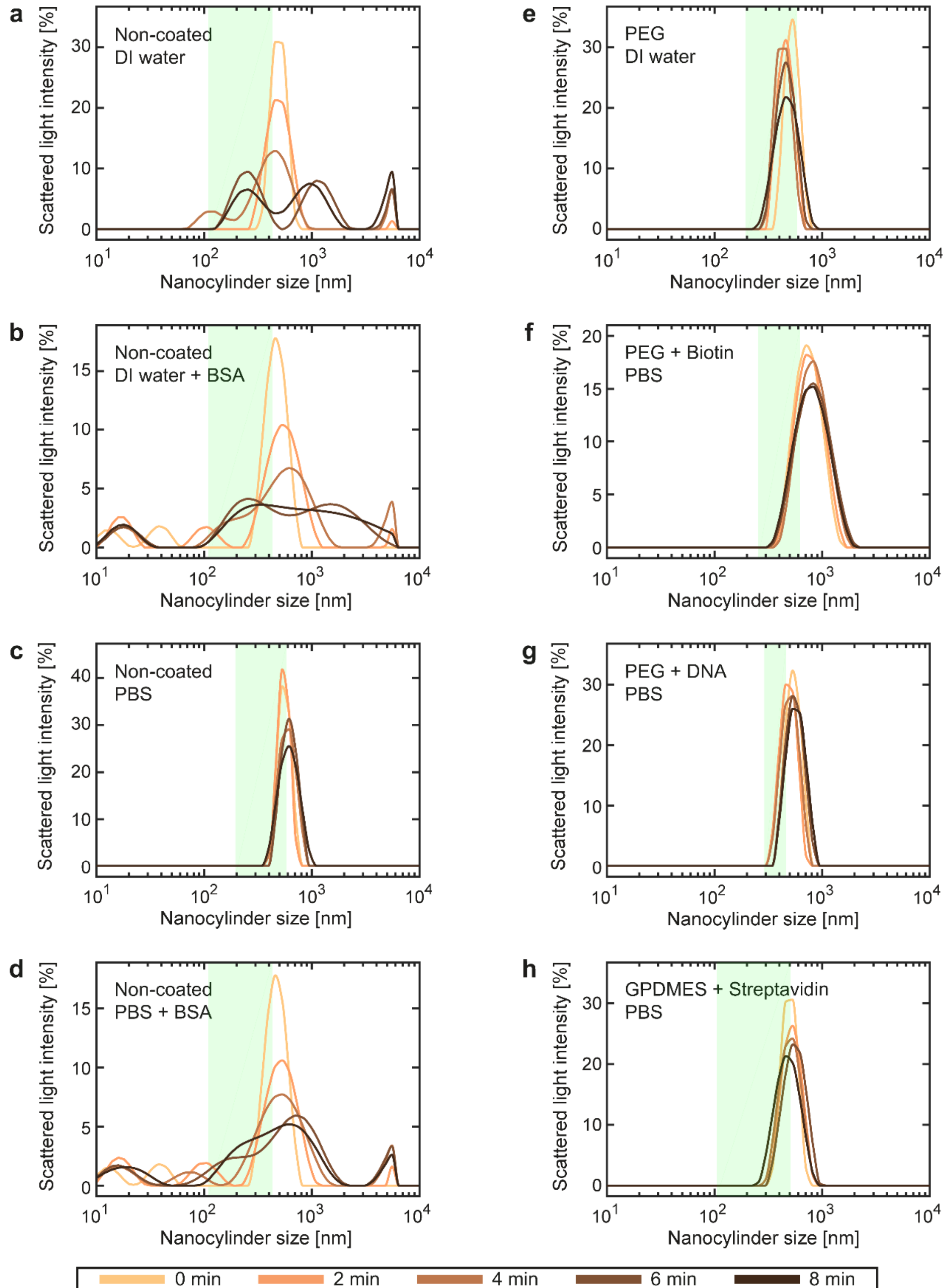

Fig. S6. DLS measurements of single-crystal TiO_2 nanocylinder aggregation in relation to surface coatings and buffer conditions. In the DLS graphs, each curve is an average of 10 measurements with a duration of 10 s each, with 2 min between successive curves (see legend at bottom of figure). Each green shaded box within the panels displays the range of nanocylinder sizes measured previously in SEM (left edge: diameter, right edge: height). Top-left corner denotes the individual test conditions, which are surface coating (1st row) and buffer solution (2nd row). **(a-d)** Results for non-coated nanocylinders dispersed in **(a)** DI water, **(b)** DI water with 2% (m/v) BSA (New England Biolabs, UK), **(c)** PBS buffer (pH 7.4), and **(d)** PBS buffer (pH 7.4) with 2% BSA. **(e-g)** DLS data for PEGylated nanocylinders in **(e)** DI water, and in PBS buffer (pH 7.4) after bioconjugation with **(f)** biotin and **(g)** DNA. **(h)** Result for GPDMES-coated nanocylinders with bound streptavidin

in PBS buffer (pH 7.4): this condition is used for the presented single-molecule OTW experiments (**Fig. 5**). The SEM-measured nanocylinder dimensions are as follows where D (H) denotes diameters (heights): **(a,b,d)** D: ~110 nm, H: ~430 nm; **(c,e)** D: ~195 nm, H: ~585 nm; **(f)** D: ~255 nm, H: ~625 nm; **(g)** D: ~290 nm, H: ~460 nm; **(h)** D: ~105 nm, H: ~505 nm.

Measurements and analysis of DLS data

We probe the aggregation of cleaved, isolated single-crystal TiO_2 nanocylinders with different surface coatings and buffer solutions via DLS (Zetasizer Nano ZS, Malvern, UK). We compare the degree of nanocylinder aggregations by characterizing the nanocylinder size distributions with 173° backscattering angle at 25 °C. To achieve monodispersed nanocylinders in aqueous solution, we vortex the nanocylinder solutions for 1 min before each measurement. However, for the nanocylinders in **Fig. S6a**† and **Fig. S6b**†, vortexing is insufficient to obtain monodispersity. For these samples, we sonicate the solutions for 10 min before measurements. We attribute the mismatch between nanocylinder dimensions (green boxes) based on SEM image analysis and size measurements via DLS to the highly scattering nature of TiO_2 and non-spherical shape of the nanocylinders. Besides the aggregated nanocylinder solutions (**Fig. S6a,b,d**†) which are apparent from the severe broadening of the size distributions, the monodispersed nanocylinder solutions (**Fig. S6c,e-h**†) exhibit only sedimentation of nanocylinders over time, observable by intensity decrease.

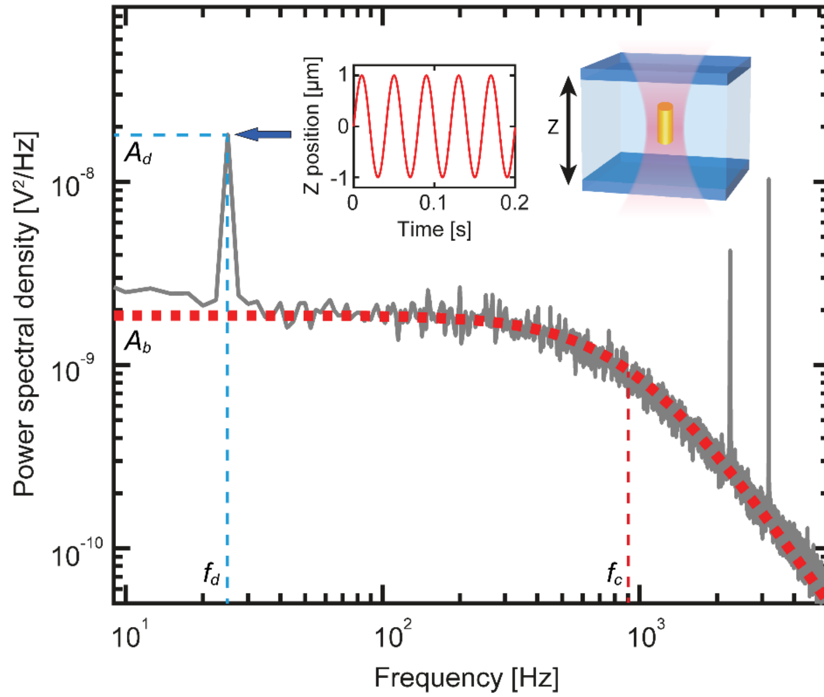

Fig. S7. Optical trap calibration of single-crystal TiO_2 nanocylinders. The power spectral density (gray curve) of a trapped TiO_2 nanocylinder with a Lorentzian fit (red dotted line) provides corner frequency (f_c) and baseline amplitude (A_b). A piezo stage drives the flow cell sinusoidally in time (with amplitude of 1 μm and frequency of 25 Hz) along the z-axis (inset) to induce a drag force to the trapped nanocylinder. The driving frequency (f_d) of this modulation appears as a spike in the power spectrum (blue arrow), with amplitude A_d. Analysis of the three measured values (A_b, A_d, and f_c) yields the three necessary parameters for the force calibration in an OTW: nanocylinder drag coefficient, PSD sensitivity, and trap stiffness.[21]

Supplementary References

1 Z. Huang, F. Pedaci, M. Van Oene, M. J. Wiggin and N. H. Dekker, *ACS Nano*, 2011, **5**, 1418–1427.
2 C. Deufel, S. Forth, C. R. Simmons, S. Dejgosha and M. D. Wang, *Nat. Methods*, 2007, **4**, 223–225.
3 P.-C. Li, J.-C. Chang, A. La Porta and E. T. Yu, *Nanotechnology*, 2014, **25**, 235304.
4 B. Gutiérrez-Medina, J. O. L. Andreasson, W. J. Greenleaf, A. Laporta and S. M. Block, *Methods Enzymol.*, 2010, **475**, 377–404.
5 J. Lipfert, M. M. van Oene, M. Lee, F. Pedaci and N. H. Dekker, *Chem. Rev.*, 2015, **115**, 1449–1474.
6 I. Steingoetter and H. Fouckhardt, *J. Micromech. Microeng.*, 2005, **15**, 2130–2135.
7 H. Chen, Q. Zhang and S. Y. Chou, *Nanotechnology*, 2015, **26**, 085302.
8 R. Janissen, B. A. Berghuis, D. Dulin, M. Wink, T. van Laar and N. H. Dekker, *Nucleic Acids Res.*, 2014, gku677.
9 J. Lipfert, D. A. Koster, I. D. Vilfan, S. Hage and N. H. Dekker, in *DNA Topoisomerases: Methods and Protocols*, ed. D. J. Clarke, Humana Press, New York, United States, 2009, Ch. 7, 71–89.
10 J. Lipfert, J. W. J. Kerssemakers, T. Jager and N. H. Dekker, *Nat. Methods*, 2010, **7**, 977–980.
11 H. Felgner, O. Müller and M. Schliwa, *Appl. Opt.*, 1995, **34**, 977–982.
12 D. A. Koster, A. Crut, S. Shuman, M.-A. Bjornsti and N. H. Dekker, *Cell*, 2010, **142**, 519–530.
13 K. Suzuki, S.-W. Youn, Q. Wang, H. Hiroshima and Y. Nishioka, *Microelectron. Eng.*, 2013, **110**, 432–435.
14 K. Mohamed and M. M. Alkaisi, *Nanotechnology*, 2013, **24**, 015302.
15 P. Yinsheng, Y. Xiaoling, X. Bo, J. Peng, N. Jiebin, J. Rui and W. Zhanguo, *J. Semicond.*, 2010, **31**, 012003.
16 R. J. Shul, G. B. McClellan, R. D. Briggs, D. J. Rieger, S. J. Pearton, C. R. Abernathy, J. W. Lee, C. Constantine and C. Barrat, *J. Vac. Sci. Technol. A*, 1997, **15**, 633-637.
17 T. Mishima, K. Terao, H. Takao, F. Shimokawa, F. Oohira and T. Suzuki, presented in part at the 24th Int'l Conf. on Micro Electro Mechanical Systems, Cancun, Mexico, January, 2011.
18 P. Kaspar, Y. Jeyaram, H. Jäckel, A. Foelske, R. Kötz and S. Bellini, *J. Vac. Sci. Technol. B*, 2010, **28**, 1179–1186.
19 S. P. Pujari, L. Scheres, A. T. M. Marcelis and H. Zuilhof, *Angew. Chem. Int. Ed.*, 2014, **53**, 6322–6356.
20 W.-J. Kim, S. Kim, B. S. Lee, A. Kim, C. S. Ah, C. Huh, G. Y. Sung and W. S. Yun, *Langmuir*, 2009, **25**, 11692–11697.
21 S. F. Tolić-Nørrelykke, E. Schäffer, J. Howard, F. S. Pavone, F. Jülicher and H. Flyvbjerg, *Rev. Sci. Instrum.*, 2006, **77**, 103101.